I.O.S.

THE TIDAL DYNAMICS OF THE WESTERN NORTH SEA

JACQUES SAUVEL

REPORT NO 138
1982

NATURAL ENVIRONMENT RESEARCH COUNCIL
INSTITUTE OF OCEANOGRAPHIC SCIENCES

INSTITUTE OF OCEANOGRAPHIC SCIENCES

Wormley, Godalming,
Surrey, GU8 5UB.
(0428 - 79 - 4141)

(Director: Dr. A.S. Laughton FRS)

Bidston Observatory,
Birkenhead,
Merseyside, L43 7RA.
(051 - 653 - 8633)

(Assistant Director: Dr. D.E. Cartwright)

Crossway,
Taunton,
Somerset, TA1 2DW.
(0823 - 86211)

(Assistant Director: M.J. Tucker)

On citing this report in a bibliography the reference should be followed by the words UNPUBLISHED MANUSCRIPT.

The tidal dynamics of the western North Sea

Jacques Sauvel

Internal Report No. 138

1982

Permanent address:
Service Hydrographique de la Marine
3 rue Octave Greard
Paris 75007
France

Institute of Oceanographic Sciences
Bidston Observatory
Birkenhead
Merseyside, U.K.

Preface

Jacques Sauvel worked at Bidston from November 1981 to February 1982 while on study leave from the French Service Hydrographique et Oceanographique de la Marine. His visit coincided with the data reduction phase of an Institute observational experiment along a coastal strip, extending from the Firth of Forth to the Humber Estuary, in the North Sea. Jacques worked on the analyses and interpretation of the current meter, bottom pressure and sea level data from this experiment, during a very active four month period; he also completed a manuscript from which this Report has been prepared.

The study of currents and elevations shows that a model of a single Kelvin wave propagation from north to south along the coast neglects a substantial standing-wave component which is found in the observations. Comparisons of current structure with existing theories and with a previously established numerical model of the area produce good agreement. Numerical model and observational estimates of energy fluxes are also in good agreement, but the flux energy budget for a particular area is very sensitive to assumptions about the interpolations made along the boundaries. In the final section Jacques develops a novel technique for computing energy losses, due to a cubic frictional dissipation law, from observations. These losses lie within the rather broad estimates of energy losses based on the flux budgets.

Full details of the observational programme are given in IOS Cruise Report Number 128.

D.T. Pugh

SUMMARY

A coastal strip 200 x 30 miles on the East Coast of England has been studied by I.O.S. Bidston.

The examination of the currents and elevations shows:

(i) there are significant differences between a model of single Kelvin wave propagation and the real tidal dynamics,

(ii) the non-progressive part of the tidal waves seem to have a prevailing direction between 53° and 67° north of east.

(iii) simple theory can explain the observed vertical structure of tidal currents in this region,

(iv) the non tidal residuals for the currents are dominated by inertial currents.

(v) the currents and elevations for M2 are in good agreement with values computed using an established numerical model.

The study of the energy budget for M2 shows:

(i) a good agreement between the values of the energy fluxes at the boundaries, and the bottom friction dissipation, from the experiments and from the model,

(ii) the sensitivity of the energy flux balance to small changes in the boundary interpolation schemes.

CONTENTS

Abbreviations throughout this report:

NSE The IOS North Sea Experiment, May-June 1981.

DNM Depth integrated North Sea Numerical model, developed by Dr A.M. Davies at Bidston. Grid size is 1/9° latitude by 1/6° longitude.

JMHP Program for calculating Kelvin wave propagation through variable bottom topography, developed by Dr J.M. Huthnance at Bidston.

NOTATION

t denotes	time .
x	eastward coordinate .
y	northward coordinate .
u	current in the x direction .
v	current in the y direction .
V	current vector (u, v) .
ω	complex current vector.
ω_+	anticlockwise rotation component of ω.
ω_-	clockwise rotation component of ω.
$\lvert\omega_+\rvert$, θ_+	modulus and argument of ω_+ .
$\lvert\omega_-\rvert$, θ_-	modulus and argument of ω_- .
ζ	surface elevation relative to undisturbed level.
G	complex surface gradient $\frac{\partial \zeta}{\partial x} + i \frac{\partial \zeta}{\partial y}$.
G_+ , G_-	anticlockwise and clockwise rotation component of .
ρ	density of the water .
a	semi major axis of the current ellipse.
b	semi minor axis of the current ellipse .
g	gravitational acceleration .
z^*	conjugate of the complex z .
$\lvert A\rvert$	modulus of A.
$\underset{\sim}{A}$	average of A over the column of water .
$\overline{A}$	average of A over a cycle.
D	depth relative to undisturbed level.
E	eddy viscosity.
L_{TOP} , L_{BOT}	current meter, at station L, nearest to the surface/bottom .

M_{UNI} only current meter at station M.

The angles are measured positive anticlockwise from geographic East (x-direction).

I INTRODUCTION

In May 1981, the Bidston laboratory of the Institute of Oceanographic Sciences performed the North Sea Experiment 1981 (henceforth: NSE). During this experiment, current meter moorings, bottom pressure recorders and coastal tide-gauges were deployed in a coastal strip 200 x 30 miles wide between the Forth and the Humber. (Figure 1).

The principal objects of the exercise were (i) to examine in detail the energetics of the tides which progress in a Kelvin-wave manner along the coast and (ii) to make an accurate hydrodynamic assessment of the variations in the mean sea surface for comparison with the standard geodetic levelling of the coastal tide gauges. This paper is concerned only with aspects of the first objective.

Tidally driven water movements dominate the physical oceanography of this part of the North Sea, with typical tidal streams of magnitude 100 cm/s and ranges of tidal elevations of 8 m. The set of data collected during NSE, provide a useful basis for a study of the major dynamic feature of this area.

In the first section of this report, we will study the tidal currents and elevations and examine the non-tidal residuals.

In the second section, we will try to evaluate energy fluxes and tidal dissipation in a similar way to the work of Taylor (1919) in the Irish Sea, and other researchers such as Robinson (1979) and Cartwright, Edden, Spencer and Vassie (1980).

II CURRENTS AND ELEVATIONS

1 Analysis of one-day current measurements

1.1 Introduction

Between 13 May and 22 May 1981, at the four stations PA, LA, HA and EA, the currents were measured in profile during 25 hours with intervals of five minutes. At each of these stations the measurements were made at five different depths (see Fig 1), by stern-anchoring the research ship RRS John Murray.

1.2 Analysis with the North Shields elevations for reference.

We assume the decomposition of the current $(u(t), v(t))$:

$$u(t) = u_0 + \tilde{a}\,\eta(t) + \tilde{b}\,\eta'(t) \qquad (1)$$

$$v(t) = v_0 + \tilde{c}\,\eta(t) + \tilde{d}\,\eta'(t) \qquad (2)$$

where $\eta(t)$ is the tide at North Shields.

We assume that this tidal elevation has the form:

$$\eta(t) = \sum_{n=1}^{N} h_n \cos(\omega_n t - \phi_n)$$

then we can define the orthogonal function:

$$\eta'(t) = -\sum_{n=1}^{N} h_n \sin(\omega_n t - \phi_n)$$

$\tilde{a}$, $\tilde{b}$, $\tilde{c}$, $\tilde{d}$ denote variables, independent of the time but dependent of the spatial position.

After making a best fit according to (1) and (2), the residuals u_0 and v_0, are always lower than 4cm/s, except at the depth 15m for the station LA where $u_0 = 5.5\,\mathrm{cm/s^{-1}}$ and $v_0 = 4.5\,\mathrm{cm\ s^{-1}}$. Their order of magnitude is small compared to the order (25cm/s) of the tidal currents.

The spatial dependent variables $\tilde{a}$, $\tilde{b}$, $\tilde{c}$, $\tilde{d}$ are generally depth-independent except at the depth 15m for the station LA and at the

depth 10m for the station EA. That shows that the tidal currents are mainly barotropic.*

1.3 Study of the ellipses of the current.

1.3.1 Approximation for the frequency.

Since we have only one day of data, we cannot separate S2 (the second largest tidal constituent) from M2 (the main constituent).

Let us assume that the motion (during 25 hours) can be approximate by a sinusoidal motion occurring at the M2 frequency:

$$\eta(t) = \sum h_n \cos(\omega_n t - \phi_n) \doteq H \cos(\omega_{M_2} t - \Phi) \quad (3)$$

and let: σ denote ω_{M_2}

t denote $t - \Phi/\sigma$, by choice of time origin.

Then

$$\eta(t) = H \cos(\sigma t)$$

$$u(t) = \tilde{a} H \cos(\sigma t) - \tilde{b} H \sin(\sigma t)$$

$$v(t) = \tilde{c} H \cos(\sigma t) - \tilde{d} H \sin(\sigma t)$$

1.3.2 Method

With the last approximation we can define w: $\quad w = u + iv \quad (4)$

with

$$\left.\begin{aligned} \tilde{\omega}_+ &= \tfrac{1}{2}(\tilde{a} + \tilde{b}) + i(\tilde{c} - \tilde{d}) = |\tilde{\omega}_+| e^{i\vartheta_+} \\ \tilde{\omega}_- &= \tfrac{1}{2}(\tilde{a} - \tilde{b}) + i(\tilde{c} + \tilde{d}) = |\tilde{\omega}_-| e^{i\vartheta_-} \end{aligned}\right\} \quad (5)$$

$$w = \tilde{\omega}_+ H e^{i\sigma t} + \tilde{\omega}_- H e^{-i\sigma t} \quad (6)$$

where $\tilde{\omega}_+$ and $\tilde{\omega}_-$ represent the anticlockwise and clockwise movements. $|\tilde{\omega}_+|$ and $|\tilde{\omega}_-|$ are their amplitudes and ϑ_+, ϑ_- are their phases.

* In this report, we use the word "barotropic", with the meaning "depth independent".

The values of the semi-major and semi-minor axes of the ellipse given by (6), are:

$$a = |\tilde{\omega}_+| + |\tilde{\omega}_-|$$

$$b = |\tilde{\omega}_+| - |\tilde{\omega}_-|$$

The orientation ϑ of the major axis is:

$$\vartheta = \frac{\vartheta_+ + \vartheta_-}{2} + K\pi$$

The main kinetic energy is: $S_t = S_- + S_+$ where S_+ is the anticlockwise energy.

$$S_+ = \frac{1}{2} H^2 \overline{\tilde{\omega}_+^* . \tilde{\omega}_+}$$

S_- is the clockwise energy.

$$S_- = \frac{1}{2} H^2 \overline{\tilde{\omega}_-^* . \tilde{\omega}_-}$$

The difference $S_+ - S_-$ is proportional to the area of the elliptical surface. Its sign is related to the polarisation of the ellipse (positive for anticlockwise). We call the ratio:

$$C_R = \frac{S_+ - S_-}{S_+ + S_-}$$

the "rotary coefficient" (Gonella (1972)). This ratio gives the partition of energy:-

$|C_R| = 1$ for pure rotary motion

$C_R = 0$ for unidirectional (or rectilinear) motion

In addition:

$$|C_R| = \frac{2ab}{a^2 + b^2}$$

For $b << a$

$$|C_R| \approx \frac{2b}{a}$$

$|C_R|$ is more sensitive to the changes of b (for b<<a), than the parameter, defined in terms of the ellipse eccentricity, ε:

$$1 - \varepsilon = \frac{2b^2}{a^2 + b^2} \approx \frac{2b^2}{a^2}$$

so we have preferred to use C_R instead of the eccentricity.

In order to appreciate the relative importance of the clockwise and anticlockwise parts, the use of $|C_R|$ is also convenient:

$$\frac{S_+}{S_+ + S_-} = \frac{1 + C_R}{2} \quad ; \quad \frac{S_-}{S_+ + S_-} = \frac{1 - C_R}{2} \; .$$

The duration τ between t = 0 and the first passage across the major axis (for $C_R \neq 0$) is:

$$\tau = \frac{|\theta_+ - \theta_-|}{2\sigma} \qquad \text{if } C_R . (\theta_+ - \theta_-) \geq 0$$

$$\tau = \frac{1}{\sigma}\left[\pi - \frac{\theta_+ - \theta_-}{2}\right] \qquad \text{if } C_R . (\theta_+ - \theta_-) < 0$$

(The angle $\sigma\tau$ will be denoted as β)

1.3.3 Results

Table 1 summarises the results of these ellipse analyses of the 25 hour data sets. It shows that:-

a) the motion is mainly barotropic

b) the major axes are parallel to the averaged coast.

c) a decrease of the clockwise part with increasing depth at the same station. The anticlockwise part remains stable. This agrees with the 3D numerical models of Davies (1982).

d) the currents are stronger at the station EA where the depth is shallower than those of the other stations.

e) the elliptical motion is anticlockwise. This sense of rotation agrees with the results from Pugh and Vassie (1976) at the Inner Dowsing.

f) the major axis rotates clockwise with increasing depth (except for the station EA).

g) the maximum currents occur earlier with increasing depth.

1.5 Study of the time of passage between two stations

We know the passage time between t = 0 and the first crossing of the current vector through the great axis of its ellipse (see Table 1). So we can deduce τ_{AB} the elapsed time between maximum currents at two nearby stations A, B (Table 2).

We can compare this time delay τ_{AB} with the propagation time τ'_{AB} of a Kelvin wave between the stations A and B, for a straight coastline:

$$\tau'_{AB} = \int_{y_A}^{y_B} \frac{dy}{\sqrt{g\,D(y)}} \qquad (7)$$

Table 2 shows this comparison.

For the transit from LA to HA, and from HA to EA, the agreement is good compared to the roughness of the approximation. For these transits, the nearby coast and bathymetry are nearly parallel.

For the passage from PA to LA, the agreement is poor. This may be due to the fact that the nearby coast is not rectilinear at all but has a complicated shape (Firth of Forth). So, for the station PA, one can consider the tide as not due to a prevailing single wave, but due to the superposition of some reflected waves (perhaps one from the SW coast, one from the NW coast, plus some Poincaré waves generated by the reflection in the corner of the Firth of Forth). (Packham and Williams, (1968)).

2. Study of the 29 days measurements

2.1 Presentation of the data

The Bidston laboratory's stock of 24 current meters, together with 7 bottom pressure recorders was deployed at the nominal positions shown in Figure 1 and in Table 3.

For our work we have used

- 17 current meters measurements

  Pairs of them were at the stations:

  H, I, L, J, N, P.

  Single meters were at the stations:

  E, F, G, K, M.

- 5 bottom pressure recorders for the stations

  E, H, J, L, P.

- 5 coastal elevation records for the stations

  Q, R, S, T, U.

All these measurements have been made for more than 29 days except the current meter measurements at K which stopped after 11.5 days and the top one at L which stopped after 25 days.

2.2 Harmonic Analysis

Tidal harmonic analysis of the East and North components of current, and of bottom pressure data were performed by the standard least squares algorithm (TIRA) used at Bidston for the routine analysis of tidal time series. Harmonic analysis assumes an elevation of the form:

$$\zeta = z_o + \sum_{n=1}^{N} f_n H_n \cos(V_n + u_n - g_n) \qquad (8)$$

(with the classical notations). With a month of data to be analysed, 26 astronomical and shallow water frequencies were incorporated into the least squares fit. But, with only one month of data, this method cannot resolve all the important components. So, 8 important components not included in these 26, have been taken into account by assuming relationships in amplitude and phase with one of the 26 major components. These relationships are deduced from nearby coastal elevation analyses for which a year's data span, and hence a full analysis, are available.

For the station K with 11 days of data, we have taken 15 major constituents and 14 related constituents.

This use, for current analysis of relations based on elevations analysis, has to be treated with caution. The response of currents to astronomical generating forces is not necessarily the same as the response of elevations, especially when there is a stratification. But this method has been shown to be satisfactory in this area (Pugh and Vassie (1976)).

The currents seem to be governed by mainly barotropic dynamics so we can assume that the knowledge of the currents at mid-depth gives a fairly acceptable idea of the profile of currents (this will be confirmed at the stations where two current meters were deployed). This feature of depth independence can be explained by the fact that the anticlockwise part of the ellipse is predominant. (See paragraph II.5 of this report and Prandle (1982)).

Tables 4a and 4b show the results of this analysis for the current meter at the station L.

Before discussing these results and studying the shape of the ellipse, it is interesting to have a look at the residuals of these analyses. Hence, we will be able to estimate the background noise and make an estimate of the error.

2.3 Study of the residuals.

The energy spectra for bottom pressure, u-currents and v-currents show the following characteristics (for example, Station L, Figures 2, 3a, 3b):

*) Clear peaks at the tidal constituents not removed by the harmonic analysis, for the bottom pressure residuals spectra, including the eighth-diurnals (Figure 2).

*) Large residuals in the currents. This spectrum has the same concave shape as the one found by Pugh and Vassie (1976).

*) The shape of the noise in the bottom pressure residual spectra is quite different and appears to be convex.

The peaks at 1.67 cpd, the inertial current frequency, exceed the noise level by more than the 95% confidence limit (Figures 3a, 3b). There is no associated peak for the bottom pressure spectra (Figure 2). A cross-correlation analysis shows that the phase difference between u and v is 90°. So, these inertial currents rotate clockwise in circular fashion in accordance with theory (Proudman (1953)).

The plots of time series for the residual currents at L_{BOT} (Figures 5a, 5b) illustrate this predominance of the inertial currents. A calculation between the troughs (1) and (2) in Figure 5b shows a length of time of about 14.5 hours between two successive troughs. (The inertial frequency corresponds to a period of 14.4 hours at 55 North).

A high coherence for the bottom pressure residuals has been found, especially at the tidal frequencies not included in our harmonic analysis. (Figures 4a, 4b, which are nearly identical). This can be explained by the low noise in the bottom pressure spectra outside the tidal bands (Figure 2).

A poor coherence has been found for:-

u- and v- components of current at the same station,

currents and elevations at the same station,

currents for two different stations.

If we estimate the standard errors according to the formula (see also Munk & Cartwright (1967)):

$$(\text{standard error})^2 = \frac{1}{2}\left(\frac{\text{residual variance}}{\text{signal variance}}\right)\left(\frac{27.3}{\text{time span in days}}\right)$$

we find the following estimates for the semidiurnal band.

0.3 cm/s for the current

0.2 cm for the elevations

These results are much lower than the confidence which is generally associated with analyses of 29 days of data, Pugh & Vassie (1976).

The under-estimate of the background residual energy may be due to the fact that our harmonic analysis has over-fitted the tidal amplitudes and so the analysis has deprived the noise of a substantial part of its energy. The numerous troughs in the spectra, specially at the frequency corresponding to the analysed tidal components, are a confirmation of this deprivation.

2.4 Shape of the ellipses.

Let us take:

$$w(t) = u(t) + i\,v(t) \tag{9}$$

So:

$$w(t) = \sum_{n=1}^{N} \left(u_n(t) + i\,v_n(t)\right)$$

$$= \sum_{n=1}^{N} \left(w_{n+}\, e^{i\sigma_n t} + w_{n-}\, e^{-i\sigma_n t}\right)$$

For each component, we can define an ellipse:

$$w_n(t) = w_{n+}\, e^{i\sigma_n t} + w_{n-}\, e^{-i\sigma_n t} \tag{10}$$

and determine its characteristics as in section 1.3. For example, Table 5 shows the results for the top current meter at Station L.

For the astronomical components whose ellipse major axis is significant (M2, S2, N2, K2, ν 2, O1, K1), the same comments apply as in section 1.3.

The calculations of the propagation time for M2, S2, O1, K1 (Table 2), are also subject to the same comments as in section 1.4.

It is also possible to look at the dispersivity of the waves. A Kelvin wave is non-dispersive, so if the dynamics are due only to Kelvin waves, we might find the same time of passage for the diurnal and the semi-diurnal bands; this is not the case between L and H but seems to be so between H and E and between P and L.

In addition, Mysak and Tang (1974) have shown that the coastal irregularities slow the speed of the Kelvin wave. We could expect a theoretical propagation time, parallel to a rectilinear coast and bottom bathymetry without irregularities, to be shorter than the real propagation time; however, this effect is not obvious in Table 2.

The ellipses at tidal frequency are mainly anti-clockwise and the ones generated in shallow waters are mainly clockwise. This is in agreement with the study of ellipse rotation at Inner Dowsing by Pugh and Vassie (1976).

For the components generated in shallow water (2SM2, MK3, MN4) the major axis does not seem to have any predominant direction. In addition, they show sometimes strong discrepancies between the top measurement and the bottom measurement. The results for the currents in these shallow water components are not reliable because of their low signal to noise ratio.

2.5 Comparison of wave propagation times.

First consider a Kelvin wave with topography. The calculations of the propagation times between two stations shows that these are consistent with the Kelvin wave speed $c=(gD)^{\frac{1}{2}}$. The direction of the major axis is parallel to the coast which agrees with the theory.

We have utilised a program of Dr J.M. Huthnance, at Bidston, based on the method of Caldwell, Cutchin and Longuet-Higgins (1972). This program computes the shape of a Kelvin wave propagating along an infinite rectilinear coast with a rectilinear bathymetry parallel to the coast.

This program produces current ellipses with an anticlockwise rotation for M2. But the observed minor axes for the real ellipses are larger (Table 6) than those predicted by the computer program (henceforth J M H P). Also, the decrease of the tidal elevations with increasing off-shore distance seems less pronounced in reality than in theory (Table 7).

For the currents, no firm conclusions may be drawn. The results for S2 are very close to those for M2.

With a flat bottom the ratio of elevation to currents for a Kelvin wave is constant:

$$\Omega = \sqrt{g/D}$$

If we take into account a rectilinear topography using JMHP, we find slightly different ratios for stations H, J, L (Table 8). However, both theoretical ratios were less than those observed.

There are other waves which might have been considered in the analysis. The Kelvin wave propagating on the East side of the North Sea

(i.e. Denmark, Norway) has a weak amplitude, and this coast is very far from our area of study. So, its influence in the area has been neglected. The study of other coastal trapped waves (shelf waves, Rossby topographic waves) was not successful. The slowness of the speed of these waves prevents the propagation of energy over long distances. To take into account Poincaré waves, was rather complicated: the best if not the only way to take these into account is to use a numerical model.

In conclusion, this study of the lines QGH and SKLJ, shows that the differences between the real dynamics and a single theoretical Kelvin wave cannot be neglected. This will be now confirmed by the study of the resolution of tides into progressive and non-progressive parts.

3. Resolution of tides into progressive and non-progressive waves.

3.1 Introduction

For a Kelvin wave propagating parallel to a straight bathymetry (hence, a straight coast), the maximum current in the direction of propagation occurs at the time of local high water.

For a tidal wave, whose currents have a phase lag of ϕ on the elevation, the averaged energy flux is proportional to $\cos\phi$. The flux is zero for $\phi = \frac{\pi}{2} + k\pi$ and a maximum for $\phi = k\pi$.

3.2 Method

Measuring times relative to local high water, let us consider the currents in a progressive wave at frequency σ_n to be given by:

$$W_p \cos \sigma_n t$$

propagating in direction λ.

Similarly, for a non-progressive wave along an axis, having a direction γ, the currents are given by:

$$W_{np} \sin \sigma_n t$$

From our own analysis, we have from (8) (9) and (10), the current W_n:

$$w_n(t) = u_n(t) + i\, v_n(t)$$

$$w_n(t) = w_{n+}\, e^{i\sigma_n t} + w_{n-}\, e^{-i\sigma_n t}$$

So:

$$w_n(t) = \cos \sigma_n t \,[w_{n+} + w_{n-}] + i \sin \sigma_n t \,[w_{n+} - w_{n-}] \qquad (11)$$

Hence, we can resolve w_n into a progressive and a non-progressive wave with:

$$w_p = |w_{n+} + w_{n-}| \quad ; \quad \lambda = Arg\,(w_{n+} + w_{n-}) .$$

$$w_{np} = |w_{n+} - w_{n-}| \quad ; \quad \gamma = Arg\, i(w_{n+} - w_{n-}) .$$

This method is the same as that used by Pugh and Vassie (1976).

3.3 Results.

The results, found at the Inner Dowsing, at the Shell-Esso platform and at station Z_o (Figure 1) by Pugh and Vassie (1976), are included in the presentation of the results for comparison. However, at these three points, the depths were shallower and the coastline shape more complicated than in our area of study.

The amplitudes and directions computed in this way are given in Tables 9a, 9b, 9c, 9d for the principal diurnal (O1, K1) and semi-diurnal (M2, S2) constituents at the five stations where have both current meter and bottom pressure measurements. From these tables we draw the following conclusions.

*) The direction of the progressive wave is the direction of the energy flux. It follows the direction of the coast (Figure 6).

*) The non-progressive part has surprisingly large amplitudes. The ratio W_{np}/W_p is greater than unity at station J. This station is far from the coast (130 km), the Kelvin waves are weak, and the effects of offshore propagating waves (such as the Poincaré waves), are more significant. This ratio W_{np}/W_p is also high at station P. This can perhaps be explained by the proximity of the Firth of Forth which would induce reflections.

*) The non-progressive part seems to have a prevailing fixed direction (between 53° and 67°), for M2.

Table 10 shows that in general the maximum currents occur before high tide.

The prevailing directions for the non-progressive waves (between 53° and 67° for M2) are very constant, even when compared with the range of the direction of the progressive part of the wave (which lie between -61° and -93°).

4. Comparison with a numerical model.

4.1 Presentation of the numerical model.

The model used was developed by Dr. A.M. Davies (1976). It represents the North Sea (Figure 7). The method used was finite difference with a fine two-dimensional grid. The sizes of the grid were

$\frac{1}{9}°$ latitude (12.247 km)

$\frac{1}{6}°$ longitude (At the latitude 55°, $\frac{1}{6}°$ longitude corresponds to 10.62 km).

The bottom friction was parameterised by a quadratic law $Ku|u|$ with K = 0.0025 everywhere except near the Dutch Coast where 0.0030 was chosen. This model was run for the M2, M4, and M6 tidal components. It

conserves mass, and the energy balance between dissipation and the net result fluxes at the outer boundaries is accurate with a relative error of 1.5%. It conforms with the numerical model of Flather (1976), which has a coarser mesh, but covers the whole area of the North-West European Continental Shelf. A detailed description of this model (DNM) has been made in Davies, (1976).

4.2 Results

Comparison for M2

The observed and computed M2 currents are shown in Tables 11a, 11b, and in Figure 8.

The agreement between the DNM and the experiment are very good if we except the Station M. For the other stations the biggest differences are:

3 cm/s for the major axis (averaged value 35 cm/s)

4 cm/s for the minor axis (averaged value 8 cm/s)

10° for the orientation of the ellipse.

Elevations are compared in Table 12, and Figure 9.

For the stations H,L,P,U,S,T, where we know the real elevations, the agreement is very satisfying. The largest differences are:

15 cm for the amplitude (average value 125 cm)

3° for the phase

The DNM amplitudes are always about 12 cm lower than the real amplitudes. Perhaps this can be explained by the fact that in the DNM the coast is represented by right-angled segments. A right-angle corresponds to the maximum loss of energy for a Kelvin wave with $\omega > f$. (Packham and Williams (1968)) So we can imagine that the model reduces unrealistically the Kelvin waves and so over-generates some Poincare waves for w>f. The

use of finite elements, particularly non uniform curved finite elements, could give a better approximation of the coast.

For Station M, there is a good agreement for the anticlockwise motion

DNM (21.2 cm/s, -131^{o})

NSE (21.8 cm/s, -129^{o})

but the clockwise motion is puzzling:

DNM: (12.7 cm/s, -9^{o})

NSE: (20.7 cm/s, 1^{o})

The observed clockwise motion at M is also the largest measured in the area. Its amplitude is nearly as high as the anticlockwise part (C_R = 0.051). This may be due to the presence of the Farne Islands near the coastal Station T. This island is effectively a strong irregularity of the coast and is not included in DNM.

The agreement between NSE and DNM results are very good except for the clockwise motion of the station M. This agreement proves that the DNM reproduces the dynamics of the studied part of the North Sea in a realistic way, even quite close to the coast, where the model would be least accurate due to having to approximate the coastline with a series of line elements.

Similar comparisons may be made for the M4 tidal constituent, using Tables 14a and 14b.

NSE and DNM produced currents of the same order of magnitude:

major axis 0.5 cm/s $\leq a \leq$ 2 cm/s

minor axis $b \leq$ 0.6 cm/s

The direction of the ellipse (clockwise or anti-clockwise) is the same except for F and for I Top. Station I and Station H dynamics seem

mainly baroclinic, and this cannot be represented by a two-dimensional model.

For elevations (Table 13) the maxima differences between NSE and DNM data are 0.5 cm for the amplitude (averaged value 2 cm) and 24° for the phase.

5. Comparison of the vertical structure of the current with analytical predictions.

5.1 Theory

The vertical structure of oscillatory tidal flows has been studied analytically (Bowden et al (1959)). This structure can be represented (Prandle (1982)) as a function of two dimensionless parameters $(\frac{\omega D^2}{E})$ and $(E\omega)^{\frac{1}{2}} / \frac{g}{3\pi} |u|$ where E is the eddy viscosity, and k is the friction constant.

This theory dealing with a linearized motion in the absence of stratification shows that the anticlockwise part varies little from sea surface to sea bed; the greatest variation is in the clockwise part

(i) the amplitude of the clockwise part decreases with the depth.

(ii) the phase varies through the vertical.

These vertical dependences can be deduced from the differential equations (Prandle (1982)) for the anticlockwise part:

$$i\,(f+\omega)\,W_+ = G_+ + \frac{\partial}{\partial z} E \frac{\partial}{\partial z} W_+ \qquad (12)$$

and for the clockwise part:

$$i\,(f-\omega)\,W_- = G_- + \frac{\partial}{\partial z} E \frac{\partial}{\partial z} W_- \qquad (13)$$

G_+ and G_- denote the anticlockwise and clockwise rotational components of the surface gradient $\frac{\partial \zeta}{\partial x} + i \frac{\partial \zeta}{\partial y}$. W_+, W_- denote the anticlockwise and clockwise rotational components. ω denotes the frequency of the

oscillation. The kind of solution of (13) depends on whether the ratio ω/f is greater or less than unity.

5.2 Agreement between theory and NSE data.

Considering the phase lag structure of the currents, we consider first the 29-day analyses.

At the latitude of the North Sea, the ratio ω/f is:

$\omega/f > 1$ for ω frequency in the semidiurnal band.

$\omega/f < 1$ for ω frequency in the diurnal band.

(f = 1.67 cpd at 55° N)

The NSE data show that the maximum current occurs earlier at the bottom current meter than at the top current meter for both M2 and S2 (Table 15). For K1 and O1, the event of maximum current happens later at the bottom current meter than at the top current meter. This agrees with the theory, but we must decompose the current in clockwise and anticlockwise part to discuss this point (Tables 16 and 17).

The modulus of the phase lag between top and bottom current meters for the anticlockwise part is less than the one for the clockwise part. This is predicted by the theory because (12) implied less than (13). The clockwise part is the dominant part for the study of the phase lag, but this clockwise part changes behaviour according to $\omega/f > 1$ or $\omega/f < 1$.

For O1 and K1, θ Top - θ Bot is generally positive (Table 16)

For M2 and S2, θ Top - θ Bot is generally negative (Table 16)

This is the qualitative reason why we find, in Table 15, that the time of the maximum current shows a difference betweeen the diurnal and the semidiurnal bands.

Turning to the analyses of the 25 hours of data, the phase structure corresponds to an anticlockwise rotation of the major axis with increasing depth, for M2. This was observed for the 25 hours of data at 5 different depths (Table 1).

If we now consider amplitudes of the current, we find that the anticlockwise part is essentially vertically independent (Table 1). However, the clockwise part decreases through the vertical. These two features agree with the theory and with the numerical model of Davies (1982).

In our area of study, the M2 current ellipses are anticlockwise at the top current meter, because of these two features these ellipses will become fatter with the depth, as shown by the values of C_R, the coefficient of rotation, in Table 1.

In conclusion, the theory enables an explanation of the features of the observed vertical structure of the current. In our area of study the current ellipse is anticlockwise, and so this theory explains why the tidal currents are principally barotropic. This would not be the case if the current ellipses were clockwise.

III TIDAL ENERGY

1. Introduction

1.1 Objectives

We shall consider the two boxes QGHLKS and SKLPNU (Fig 1). We intend to calculate the water flux and the energy flux through the boundaries of these two boxes, for the component M2 only.

The calculations of the water flux will permit us to see how the water is conserved in our calculations. From the energy fluxes, we shall estimate the energy budget. This will be compared with the estimate of energy dissipation obtained from parametrization of the bottom friction.

1.2 Equations

The appropriate energy balance equation governing a region (Garret (1975)) is:

$$-\rho \int_{\Gamma} g h \, \overline{u.\zeta} \cdot \vec{n} \, ds + \rho \int_{\Gamma} g h \, \overline{u.\zeta_\epsilon} \cdot \vec{n} \, ds + \rho \int_{\Delta} g \, \overline{\zeta_\epsilon \cdot \frac{\partial \zeta}{\partial t}} \, dA \qquad (14)$$

$$= \rho \int_{\Delta} \overline{F.u} \, dA$$

with $\vec{n}$ the outward normal to a length element ds of the open boundary Γ of the sea area Δ of which dA is an element.

The first term of equation (14) corresponds to the apparent energy flux carried by a tidal wave into the area. It is the flux of potential energy measured relative to the sea-bed.

The second term corresponds to a correction to the first term (Robinson (1979)): the term $-\rho \int_{\Gamma} g h \, u.(\zeta - \zeta_\epsilon)$ is the flux of potential energy measured relative to an equipotential surface.

ζ_ϵ represents $\zeta_e + \zeta_t + \zeta_l$

with ζ_e = equilibrium tide

ζ_t = body tide

ζ_ℓ = tidal loading

The effect of the ocean self attraction can be neglected (Robinson (1979))

The third term corresponds to the rate of working of the tide-generating forces.

The fourth term corresponds to the frictional dissipation term. We assume that all the dissipation is due to bottom friction, although there may be sources or sinks of energy, such as vortex shedding at coastal headlands, and internal tides.

Taylor (1919) parameterized bottom friction by a quadratic law $K\rho \underset{\sim}{u}|\underset{\sim}{u}|$ because of the turbulence of the motions of the sea. His estimate of the tidal dissipation for the Irish Sea, was extended to all oceans by Jeffreys (1921), Heiskanen (1921), and more recently, by Miller (1966). K is an empirical constant with published estimates ranging from 0.0018 to 0.0030.

For a rectilinear stream of the form $u = u_o \cos(\sigma t - \phi_o)$ where σ is the dominant frequency, we have

$$\overline{F.u} = \frac{4}{3\pi} K \rho u_o^3$$

(The average value of $\cos^3 \sigma t$ taken without regard to sign is $\frac{4}{3\pi}$.)
The regional use of this quadratic law over a spring-neap tidal cycle is only approximate (Pugh (1981). Also, according to some authors (Wolfe (1980)) the friction parameter K can depend on the frequency.

In this paper we shall not elaborate upon the value of K. However, it is worth noting that dynamically, increasing K does not mean always

increasing the dissipation: increasing K means increasing the bottom friction which leads to a slowing of the currents, so for certain areas of the North West Continental shelf, Flather has found with numerical modelling that increasing K reduces the dissipation (Flather, personal communication).

1.3 Interpolation Procedure

In order to calculate an integral $\int_{\Gamma} f(u, v, \zeta, x, y)\, ds$, we need to estimate the function along Γ

To do this, we need to interpolate and extrapolate currents and elevations from the values at the measurement stations, along the boundaries of our two boxes.

Three ways of interpolating are possible:

i) linearly (the simplest way)

ii) using a theoretical scheme (unattractive because poor agreements were found in II 2.5).

iii) using a numerical model (attractive because of the agreements found in II.4)

Any interpolation scheme must satisfy the following constraints:

*) conserve the water .

*) verify a null cross shore speed at the coast.

*) ensure an energy loss in each of these boxes.

This last condition is due to the fact that in equation (14), the second and third terms are small compared to the dissipation term because the boxes are small and situated in shallow waters. (90 m maximum depth).

2. Methods for the calculation of energy flux.

This involves the calculation of the first term of (14). We intend to calculate these fluxes with two separate methods and so to compare their results and their limits of confidence. These two methods are: a) the use of mixed linear and theoretical interpolations with NSE data, and b) the use of the DNM data. Having compared the results of these two independent methods, we will be able to define a better approach using NSE data and interpolating with the help of the numerical model.

First method: a) use of a "mixed linear theoretical" interpolation.

This method deals with NSE data. It is independent of the numerical model. In order to decide where to choose a linear interpolation and where to choose a theoretical wave interpolation, we must first examine the data we use. Paragraph 2.5 has shown that for the ratios of minor axis/major axis and elevation/current, the comparisons between theory and these data were not satisfactory.

In addition, for the boundary UNP, the dynamics are obviously not due only to a single wave, because of the shape of the nearby coast (see: II 1.4) and II 2.4)). Moreover, if we try to adjust a Kelvin wave for the data of the elevations at S and L we find an error at the station J which is larger than the error found when taking a linear interpolation between S and L and extrapolating it to J.

In conclusion, for the boundaries SKL and QGH, a linear interpolation seems to be better adapted than any Kelvin wave approximation.

For the boundaries UNP, PL and HL, a linear approximation is the best available for this first method.

We decided to try a linear approximation first; where this fails, we shall use a Kelvin wave approximation.

2.2 Water Budget

Let us choose a linear approximation for the elevations (amplitude and phase) and for the normal velocities (amplitude and phase) to the open boundaries, from the NSE data (dashed lines in Figures 8 and 9). We are thus able to calculate the interpolated and extrapolated fluxes (dashed lines in Figure 10). In the water budget so obtained (Figure 11, Table 18a) we see:

- poor conservations of water mass in each box QHLS and SLPU
- a surprisingly accurate conservation for the whole box QHLPU

So, for the whole box QHLS, the water is conserved with an accuracy of 4% which is much better than the precision of the measurements.

For the boxes SLPU and QHLS the non-conservation of the water occurs for about 15% of the flux. This total equilibrium and these two local discrepancies suggest that the flux on the line SKL was not well estimated. We therefore changed it with the use of a theoretical Kelvin wave shape. If we adjust this approximation with the value of the current at L, the water mass is conserved (Table 18b) with a good precision but the energy budget is unrealistic: there is no energy loss in the box SLPU (Table 19a). So, neither this Kelvin wave approximation nor the linear one is satisfactory for the boundary SKL.

2.3 Cross-shore zero flow condition

The boundaries SKL, OGH and UNP are perpendicular to the coast. In our interpolation we deal only with speeds normal to the boundary, so, in our interpolations for the normal speed at the boundaries to calculate the flux, this cross shore current condition is not violated.

2.4 Energy flux

The energy fluxes are given in Figure 12, for M2. As a comparison, the S2 apparent energy fluxes are given by Figure 13. We shall not elaborate upon the transmission and dissipation of tidal energy for S2, except to note that we cannot study S2 independently from M2 because of the size of the interaction terms (see Pugh, (1981)). Energy fluxes at each frequency are additive (Pugh & Vassie, 1976), but dissipations according to cubic laws are not.

If we return to M2, from Figure 13 and Tables 19a and 19b, it can be seen that:

*) there are positive budgets for the linear interpolations and extrapolations for QHLS and SLPU. But with this method, the water is not conserved (error about 15%). So, the results on the budget are not reliable.

*) there are negative budgets for the box SLPU with a Kelvin wave approximation along SKL. This failure has already been discussed.

*) for the whole box QHLPU, the water is conserved. So, we can expect that 0.11×10^{10} W is not too far from the real budget, but we cannot ascertain the magnitude of the error.

2.5 Importance of the depth profiles.

The value of the water flux across the boundary Γ is:

$$\rho \int_{\Gamma} u \zeta \cos(g_u - g_\zeta)\, ds$$

(averaged over one tidal period of the studied harmonic, i.e. M2).

The value of the energy flux across Γ is:

$$\rho \int_{\Gamma} g\, u\, \zeta\, D \cos(g_u - g_\zeta)\, ds .$$

The water flux averaged over one tidal period is independent of the depth. The corresponding energy flux is quite sensitive to the choice of the depths.

Example

We decided to choose for SKL, the broken-line profile of the depths instead of the dashed one which is the real one.

Obviously the water budget remains the same. The energy flux (Figure 14) has the same order of magnitude but the net result of the budget (Table 20) is very sensitive to this change of depths. This happens because this net result is due to the small difference between two large numbers. This shows how the net result of the energy budget is unreliable.

3. Comparison for the energy flux from DNM with NSE data, using the mixed linear/theoretical interpolation.

3.1 DNM calculations. This numerical model conserves water mass. It also ensures zero cross-shore velocity at the coast.

3.2 Comparison of the results

*) The DNM and NSE values for the energy fluxes are very close. (Figure 16).

*) the resulting budgets for the whole area have the same order of magnitude (0.11×10^{10} W for NSE and 0.12×10^{10} W for DNM). But, this excellent agreement may be fortuitous, when one considers the size of the errors.

We shall show later that 0.12×10^{10} W must be replaced by 0.07×10^{10} W for the DNM results because of the non-parallelism between the lines of the DNM and the boundaries used for the NSE.

The estimations of the NSE energy budget have wide error bounds.

3.3 Difficulties in this comparison.

The lattice of the model (Figure 7) does not represent the real coast. Because of the use of finite differences, the DNM coast has a stepped shape. Therefore if a boundary of NSE arrives at the coast at a grid corner, the DNM corresponding line can be larger or smaller than the real one. See Figure 18. A further difficulty arises because the lines of the DNM lattice are not parallel to the lines of the NSE boxes (Table 21).

The adjustments for these difficulties do not change the order of magnitude of the fluxes, but they can change the flux budgets which are small compared with the fluxes themselves. For example an attempt to correct for line length with the formula:

$$\text{corrected flux} = \frac{\text{(length of the real line)}}{\text{(length of DNM line)}} \times \text{DNM flux}$$

implied little change for the value of the fluxes, but it considerably affected the results for the flux budget.

The DNM depths are averaged over one grid (about 12 x 10 km); this difference from the real ones does not ease the comparison between the two sets of energy fluxes (Figure 14).

3.4 Use of DNM data with the linear approximation method.

In order to compare DNM and NSE data for currents and elevations, we used DNM data with the linear approximation method. We obtained the corresponding energy fluxes (Figure 16).

These fluxes are mainly lower than the ones with NSE data (Figure 12). This fact is perhaps because amplitude of the elevations are lower in DNM data than in NSE data (Figure 9).

The flux 0.88×10^{10} W for the line UNP is greater than from the NSE (0.77×10^{10} W). This is due to the fact that the DNM currents at station N is stronger than the NSE's one. So the extrapolation from N to the coast gives quite different results.

4. Bottom Friction Dissipation

This involves the calculation of the right hand side of equation (14).

4.1 Introduction

We parameterise the bottom function dissipation with a quadratic law ($F = K u|u|$, as outlined in III 2.1).

So, we need to calculate the integral

$$I_d = \frac{1}{T}\int_0^T\int_\Delta K\rho\,|u|^3\,dA\,dt$$

i.e.

$$\frac{1}{T}\int_0^T\int_\Delta K\rho\,\left(a^2\cos^2\sigma t + b^2\sin^2\sigma t\right)^{3/2}\,dA\,dt$$

(where a is the semi-major axis and

b is the semi-minor axis)

We shall use two ways to calculate I_d. The first one is to interpolate the currents linearly over triangles which cover our area, and then to estimate the integral with these interpolated currents. The second one is the value obtained from the DNM.

4.2 Method using a linear interpolation with NSE data.

First we make the calculation over a triangle

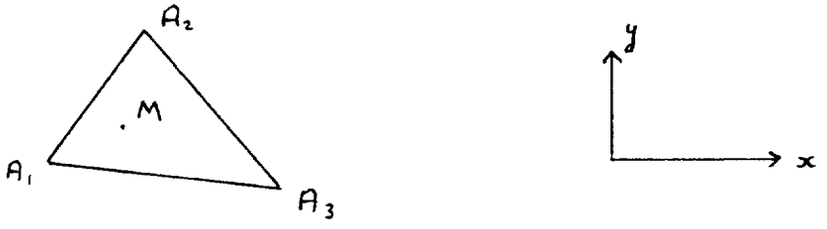

Let us assume that we know the value of some scalar function G(x,y), at each corner. We decide to interpolate G over this triangle with the function G_i:-

$$G_i(M) = P_1\ G(1) + P_2 G(2) + P_3\ G(3)$$

where (P_1, P_2, P_3) are the barycentric coordinates of M

Let us take some polynomial $\underset{\sim}{P}$, and let us suppose that we want to estimate

$$\int_{\Delta A_1 A_2 A_3} \underset{\sim}{P}\ (G(x,y))\ dA$$

In order to do so, we first approximate G by G_i. Then it is possible to integrate $\underset{\sim}{P}(G_i(P_1,P_2,P_3))$ over the triangles. For example $P(x) = x^3$. So:

$$\int G^3\, dA \approx \int G_i^3\, dA = \int \left(\sum_{i=1}^{3} P_i\ G(A_i)\, dA = S_f.\ Q\left(G(A_1), G(A_2), G(A_3)\right)\right.$$

with:

$$Q(X_1, X_2, X_3) = \frac{1}{10}\left[\sum_{1 \le i \le j \le k \le 3} X_i . X_j . X_k \right]$$

and where S_f denotes surface of the triangle A_1, A_2, A_3.

An estimation of the error due to approximating G by G_i, in the integral calculation, can be made if we know the maxima of the variations of G.

For a studied area A_Ω we first approximate it by triangles, at the corners of which the values of G are known, and we approximate G with the function $\tilde{G}$ (for which $\tilde{G}$/Triangle$(A_1\ A_2\ A_3) = G_i$).

Along any side of a triangle incorporated in the lattice covering A_Ω, this approximation of G is reduced to a linear interpolation between the values of G at the two corners of this side. This treatment is consistent with the interpolations we have previously made for the fluxes. This also ensures that G_i is a continuous function over the area.

We turn now to the estimation of the bottom friction over a triangle. At this stage, another difficulty occurs: we are not able to integrate

$$\int_0^{2\pi} (a^2 \cos^2\vartheta + b^2 \sin^2\vartheta)^{3/2}\, d\vartheta$$

analytically and so we proceed to bracket the value of this integral:

For $\vartheta \in (0, \frac{\pi}{2})$

$$(a^2\cos^2\vartheta + b^2\sin^2\vartheta)\, a\cos\vartheta \leq (a^2\cos^2\vartheta + b^2\sin^2\vartheta)^{3/2} \leq (a^2\cos^2\vartheta + b^2\sin^2\vartheta)(a\cos\vartheta + b\sin\vartheta)$$

$$f_{1_{ab}}(\vartheta) \qquad f_{0_{ab}}(\vartheta) \qquad f_{2_{ab}}(\vartheta)$$

So, we shall bracket the integral $\frac{1}{T}\int_0^T f_{0_{ab}}(\sigma t)\, dt$ with:

$$\frac{4}{T}\int_0^{T/4} f_{1_{ab}}(\sigma t)\, dt \leq \frac{1}{T}\int_0^{T} f_{0_{ab}}(\sigma t)\, dt \leq \frac{4}{T}\int_0^{T/4} f_{2_{ab}}(\sigma t)\, dt$$

$I_{1_{ab}}$ $\qquad$ $I_{0_{ab}}$ $\qquad$ $I_{2_{ab}}$

$I_{1_{ab}}$ and $I_{2_{ab}}$ are polynomials of (a, b). So, we will be able to use for them, the method described in II 4.2. We cannot make a limited expansion of $F_{a,\vartheta}(b) = f_{0_{ab}}(\vartheta)$ in the variable b for any $\vartheta \in [0, \frac{\pi}{2}]$ but we can develop the integral $I_{0_{ab}}$ in the following way:

$$4\int_0^{\frac{\pi}{2}} (a^2\cos^2\vartheta + b^2\sin^2\vartheta)^{3/2}\, d\vartheta = 4\int_0^{\frac{\pi}{2}} (a^3\cos^3\vartheta + 3ab^2\cos\vartheta\sin^2\vartheta)\, d\vartheta + O(ab^4) + O(b^3)$$

so we can approximate I_{0ab} by I_{3ab}, where: $I_{3ab} = 4\int_0^{\frac{\pi}{2}} (a^3\cos^3\vartheta + 3ab^2\cos\vartheta\sin^2\vartheta)\, d\vartheta$

As a comparison, we can define $I_{4ab} = \int_0^{2\pi} a^3\, |\cos^3\vartheta|\, d\vartheta$, which correspond to a rectilinear motion.

$I_{3_{ab}}$ and $I_{4_{ab}}$ are polynomials of (a, b). We can now proceed to to use for these polynomials the method of II 4.2, and to estimate the dissipation due to the bottom friction, with these approximations.

We do this over the area O G H L P M U, in the following stages.

1st step: approximation of the area. We know the current at 8 points GHIKLMNP, so we can define 6 triangles (Figure 17). To fit the coastline, we can define the 8 further triangles.

2nd step: calculate the bottom friction dissipation with the use of the method described above for the triangles numbered 1 to 6.

3rd step: estimation of the values of the current at the points Q, R, S, T and U. For Q and U, we use the linear extrapolation already utilised in the calculations of the flux. For R, S and T, we estimate the currents from the knowledge of the elevations at these points and from the comparisons with the data at nearby points. In any case, the cross shore current at the coast (i.e. minor axis of the ellipse) is assumed to be zero.

4th step: calculation of the bottom friction dissipation for the coastal triangles

It is necessary to consider the errors due to the neglecting of the minor axis of the ellipse. The resulting bracketing and estimation of the bottom friction dissipation (for K = 0.0025) are shown in Table 22a. These different results allow us to appreciate the size of the error committed when the small axis is neglected. Neglecting the small axis for the current ellipse, in the computation of friction dissipation happens often. When the ellipse is quite fat, some allowance for K are made in order to account for this fatness (Robinson (1979). Table 22a gives an idea of the associated error. The weights of the different terms (a^i, b^j) are shown in Table 22b.

The values for the solid triangles area are more reliable because the currents have been measured during NSE at each summit of the triangles. We conclude that the error due to this neglect of the small axis is less than 5%. This is less than the errors due to the assumption of depth independent flow and the fact that our interpolation was linear. Therefore either of the two sets of estimates in Table 23 may be used.

The published values of K range between about 0.002 and 0.003, thus implying the following range for the estimation E_s of the bottom friction dissipation.

0.06×10^{10} W < Es < 0.09×10^{10} W

4.3. Comparison with DNM results

DNM uses $K = 0.0025$ for our part of the North Sea. In order to have a coherent comparison, Table 24 shows DNM and NSE estimates of the bottom friction with $K = 0.0025$ for the two estimates. Actually, that means that we compare the integrals.

$$\int_{Box} u^3 \, dA \qquad \text{for DNM and NSE.}$$

The agreement in Table 24 is remarkably good if we think we have used two completely separate methods (for further elaboration see Davies, Sauvel and Evans (1982)).

Finally, we consider the error due to the non parallelism between the DNM lines and the boundaries of the boxes of the NSE. DNM ensures a balance between the net energy flux (R1) and the dissipation due to bottom friction (R2). This kind of dissipation is the only one allowed in the DNM. We found:

R1 = 0.12×10^{10} W

R2 = 0.07×10^{10} W

This difference, 0.05×10^{10} W, between R1 and R2 may be due to the approximations made for the calculation of DNM energy flux. These approximations were necessary because of the non parallelism of DNM lines and the boundaries of the box OHLPUS monitored by the NSE.

5. Discussion

5.1. Energy balance equations

In III 1.2 we have introduced the equation (14):

$$-\rho\int_{\Gamma} gh\,\overline{u.\zeta}.\vec{n}\,ds + \rho\int_{\Gamma} gh\,\overline{u.\zeta_\varepsilon}.\vec{n}\,ds + \rho\int_{\Delta} g\,\overline{\zeta_\varepsilon.\frac{d\zeta}{dt}}\,dA = \rho\int_{\Delta}\overline{F.u}\,dA$$

(with $\vec{n}$ the outward normal to an element ds of the open boundary Γ of the sea area Δ of which dA is an element).

In III 2 and III 3, we have computed the term $\int gh\,\overline{u.\zeta}\,n\,ds$.

In III 9 we have calculated the bottom friction dissipation $\rho\int_{\Delta}\overline{F.u}\,dA$.

Our area under study is relatively small: 70 x 200 km . So the effects of direct astronomical forcing and earth tides are small compared to the effects of bottom friction. This point has been illustrated by the studies of the Gulf of California (Filloux, 1973) and of the Irish Sea (Robinson, 1979). So, we can suppose that these terms are small. Equation (14) is reduced to an equilibrium between the two computed integrals. From our previous calculations, we are now able to compare these two terms.

5.2 Disagreement in the energy balance.

If we maximise the estimated bottom friction dissipation with the use of $K = 0.003$, we find for NSE data a value equal to 0.09×10^{10} W for the whole area. This value is less than 0.11×10^{10} W which is the net result of the energy flux computed in III 2.

5.3 Possible explanations.

We have made many approximations in the calculations of the flux, so when we deduced the net budget from the influx and the outflux, these approximations can completely change the result. If the approximations

lead to a systematic error (for example, underestimation of the currents at the coast), the net budget will not be too much affected. If these errors are random, the net budget will be much less uncertain.

The estimation of the dissipation by $k\rho u|u|$ may not be appropriate for the dynamics very close to the coast. The effects of large shear velocities,and of irregularities in the coastline (islands, headlands) increase this dissipation. There is also some transfer to internal tides because of the topography of the sea bottom, but this report cannot prove anything about it because of the size of the errors in the net result for the energy flux balances.

5.4. Other investigations.

The same comparisons for the boxes QHLS and SLPU are not possible, because we have seen that the flux at the boundary SKL is imprecise. The study of the box GHLPNMKIG could have been worthwhile because this area corresponds to the solid triangles, where the estimation of the bottom friction is more precise. Further, this area is more than 30 km off the coast so is not complicated by the coastal boundary layer (about to 10 km off the shore). However, sizes of the errors in the net result of the fluxes are too big to prove anything.

5.5. Improved method.

Wherever we were able to compare NSE data and DNM results for M2, the agreement was generally very good. So, one can imagine that, inside our area of study, DNM results are generally very close to reality. So, the best way to extrapolate NSE data is to use the relative shape of the currents and of the elevations. In order to ease this use of relative shape at the boundaries of the box, it would be useful to have the lines

of the grid of the numerical model, parallel to the boundaries of the boxes. As these boundaries are not a set of parallel and perpendicular lines, the use of finite elements would be interesting. The use of finite elements, especially curved finite elements would also be useful to represent the coastline, particulary for features like the Farne Island, and to represent the bathymetry. Therefore, this mixed method utilising both NSE data and a numerical model would enable a better value of the fluxes and of the bottom friction dissipation to be obtained.

Acknowledgements.

I would first like to thank Dr. Cartwright, Assistant Director of the Institute of Oceanographic Sciences for inviting me to spend four months at I.O.S. (Bidston) and for supervising the work.

I am grateful to the Service Hydrographique and Oceanographique de la Marine and to the Delegation Generale de l'Armement for granting me paid leave of absence.

I would like also to thank specially Dr. Pugh for providing the data, his constructive criticism, and help for the writing of the script.

I am also indebted to Drs. Davies, Huthnance, Prandle, Thompson, Vassie, Alcock and Howarth for various helpful discussions during the course of this work.

The staff at Bidston were very supportive during my stay, and, for this, I am very grateful. In particular I would like to thank David Ovadia for his infinite patience with my computing problems and Hilary Faull for her good mood.

Finally, a special thanks to those who typed this manuscript, and drew the figures.

References

BOWDEN, K.F., FAIRBAIRN, L.A. & HUGHES, P. 1959 The distribution of shearing stresses in a tidal current.

Geophysical Journal of the Royal Astronomical Society, 2, 288-305.

CARTWRIGHT, D.E., EDDEN, A.C., SPENCER, R. & VASSIE, J.M. 1980 The tides of the North East Atlantic Ocean.

Philosophical Transactions of the Royal Society of London, A, 298, 87-139.

CALDWELL, D.R., KUTCHIN, D.L. & LONGUET-HIGGINS, M.S. 1972 Some model experiments on continental shelf waves.

Journal of Marine Research, 30, 39-55.

DAVIES, A.M. 1976 A numerical model of the North Sea and its use in choosing locations for the deployment of offshore tide gauges in the Jonsdap '76 oceanographic experiment.

Deutsche Hydrographische Zeitschrift, 29, 11-24.

DAVIES, A.M. 1982 A three dimensional tidal model of the North West European continental shelf with application to the M4 tide. (in press).

DAVIES, A.M., SAUVEL, J.S. & EVANS, J.J. On computing tidal energy dissipation from observations and a numerical model (in preparation).

FILLOUX, J.H. 1973 Tidal patterns and energy balance in the Gulf of California.

Nature, 243, 217-221.

FLATHER, R.A. 1976 A tidal model of the north west European continental shelf.

Mémoires de la Société royale des Sciences de Liège, 6 ser., 10, 141-164.

GARRETT, C.J.R. 1975 Tides in gulfs.
Deep-Sea Research, 22, 23-35.

GONELLA, J. 1972 A rotary-component method for analysing meteorological and oceanographic vector time series.
Deep-Sea Research, 19, 833-846.

HEISKANEN, W. 1921 Uber des Einfluss der Gezeiten auf die Sakulaire acceleration des Mondes.
Annales Academiae scientiarum fennicae, A, 18, 1-84.

JEFFREYS, H. 1921 Tidal friction in shallow seas.
Philosophical Transactions of the Royal Society of London, A, 221, 239-264.

MILLER, G.R. 1966 The flux of tidal energy out of the deep oceans.
Journal of Geophysical Research, 71, 2485-2489.

MUNK, W. & CARTWRIGHT, D.E. 1967 Tidal spectroscopy and prediction.
Publications Scientifiques, Association Internationale d'Océanographie Physique, 27, 193-242.

MYSAK, L.A. & TANG, C.L. 1974 Kelvin wave propagation along an irregular coastline.
Journal of Fluid Mechanics, 64, 241-261.

PACKHAM, B.A. & WILLIAMS, W.E. 1968 Diffraction of Kelvin waves at a sharp bend.
Journal of Fluid Mechanics, 34, 517-529.

PRANDLE, D. 1982. Vertical current structure for tides and other oscillatory flux. (in press).

PROUDMAN, J. 1953 Dynamical oceanography. London: Methuen. 409pp.

PUGH, D.T. & VASSIE, J.M. 1976 Tide and surge propagation off-shore in the Dowsing Region of the North Sea.

Deutsche Hydrographische Zeitschrift, 29, 163-213.

PUGH, D.T. 1981 Tidal amphidrome movement and energy dissipation in the Irish Sea.

Geophysical Journal of the Royal Astronomical Society, 67, 515-527.

ROBINSON, I.S. 1979 The tidal dynamics of the Irish and Celtic seas.

Geophysical Journal of the Royal Astronomical Society, 56, 159-197.

TAYLOR, G.I. 1919 Tidal friction in the Irish Sea.

Philosophical Transactions of the Royal Society of London, A, 220, 1-93.

WOLF, J. 1980 Estimation of shearing stresses in a tidal current with application to the Irish Sea.

pp.319-344 in, Marine turbulence, (ed.J.C.J.Nihoul). Amsterdam: Elsevier. 378pp.

Station HA		B_+	ϕ_+	B_-	ϕ_-	GA	SA	Rotation Coefficient	Direction (E + ve) of major axis	β
21 May 81										
D 1	15	0.13	-70°	0.13	-36°	0.23	0.04	0.34	-53°	17°
D 2	30	0.14	-84	0.09	-50	0.22	0.05	0.44	-66	17
D 3	45	0.14	-78	0.06	-71	0.20	0.07	0.67	-75	3
D 4	56	0.13	-75	0.05	-84	0.18	0.08	0.76	-80	175
D 5	66	0.12	-90	0.06	-45	0.18	0.06	0.63	-67	22
average		0.12	174	0.07	-50	0.19	0.06	0.55	-64	14
Station EA										
D 1	10	0.22	-119	0.18	-15	0.40	0.05	0.24	-67	52
D 2	20	0.20	-105	0.10	-20	0.30	0.10	0.60	-63	42
19 May 81										
D 3	30	0.20	-104	0.08	-29	0.29	0.13	0.73	-66	37
D 4	37	0.20	-158	0.16	-35	0.26	0.14	0.82	-68	33
D 5	42	0.18	-98	0.04	-24	0.23	0.13	0.86	-61	37
average		0.19	-108	0.10	-20	0.29	0.09	0.56	-64	44
Station LA										
D 1	15	0.15	-54	0.10	-63	0.25	0.04	0.36	-59	175
D 2	31	0.15	-62	0.08	-67	0.22	0.07	0.58	-64	177
13 May 81										
D 3	45	0.14	-58	0.07	-70	0.22	0.07	0.57	-64	173
D 4	55	0.14	-63	0.07	-81	0.20	0.06	0.56	-73	171
D 5	65	0.13	-58	0.04	-90	0.18	0.09	0.80	-75	164
average		0.14	-58	0.08	-69	0.21	0.06	0.53	-64	175
Station PA										
D 1	10	0.13	-37	0.11	-126	0.24	0.02	0.17	-81	136
D 2	20	0.13	-39	0.08	-165	0.21	0.05	0.41	-102	116
D 3	30	0.12	-40	0.07	-171	0.19	0.05	0.56	-105	115
15 May 81										
D 4	44	0.13	-39	0.06	-170	0.19	0.07	0.63	-105	114
D 5	54	0.12	-34	0.05	-173	0.16	0.07	0.73	-104	110
average		0.12	-38	0.07	-153	0.18	0.05	0.52	-96	122

Table 1 Summary of current ellipse analyses of 25 hours of profiling data. B_+ and B_- are anticlockwise and clockwise response amplitudes to the simultaneous tidal elevations at North Shields. ϕ_+ and ϕ_- are the corresponding phases. GA and SA are the directions (relative to geographic east) of the major and minor current ellipse axes respectively; β is the phase angle between $t=0$ and the time of flow along the major axis. Depths are in metres.

Path	Travel distance (Km)	Theoretical times $(gD)^{\frac{1}{2}}$ for a flat bottom	Theoretical times $(gD)^{\frac{1}{2}}$ with topographic adjustments	Theoretical times $(gD)^{\frac{1}{2}}$ Currents (25 hours)	Observed times Currents (29 day analyses)				
						M2	S_2	O_1	K_1
P to L	120	1.31	1.31	1.80	1.78	(top pair)	1.94	1.35	2.43
					1.66	(bottom pair)	1.64	1.88	1.67
					1.72	(average)	1.79		
L to H	74	0.76	0.76	0.66	0.51	(top pair)	0.34	0.29	0.22*
					0.75	(bottom pair)	0.71	0.24*	0.60*
					0.63	(average)	0.52		
H to E	87	1.01	1.04	1.06	1.01		0.93	0.98	1.11

Table 2. Comparison between theoretical and observed wave propagation times in hours between two adjacent Stations.

(*these times have been corrected to take into account the non parallelism of the major axis at the two Stations)

Station	Latitude	Longitude	Depth (below) ACD) m	Spring Tidal Range m	Maximum Spring Tidal Current	OSTG	Current Meters	Thermistor Chains	Current Meters above bed (m)
E	54° 00'N	0° 50'E	48	4	0.5	TG(DQ)	1	25m	30
F	54° 20'N	0° 30'E	58	4	0.8		1		25
G	54° 38'N	0° 12'W	60	4	0.8		1		30
H	54° 48'N	0° 15'E	77	3.5	0.7	TG(SG)	2		25 50
I	54° 56'N	0° 30'W	60	4	0.8		2		20 40
J	55° 35'N	0° 45'E	75	2.5	0.5	TG(DQ)	2		25 50
K	55° 10'N	1° 00'W	86	4	0.6		1		35
L	55° 19'N	0° 33'W	70	4	0.6	TG(SG)	2	50m	25 50
M	55° 42'N	1° 13'W	73	4	0.8		1		35
N	56° 04'N	1° 45'W	50	4	0.8		2		15 30
P	56° 16'N	1° 12'W	60	3.5	0.5	CM/TG	2	50m	20 40

Table 3. Nominal positions of the rigs deployed by the John Murray, Spring 1981. Detailed positions of actual deployment are given in the IOS Cruise Report.

RELATED CONSTITUENTS

RELATED CONST.	REFERENCE CONST.	H (m/s)	G (°)
PI1	K1	0.009	230.3
P1	K1	0.045	218.0
PSI1	K1	0.006	66.0
PHI1	K1	0.009	3.3
2N2	N2	0.024	77.0
NU2	N2	0.053	96.7
T2	S2	0.021	157.2
K2	S2	0.116	156.2

MAJOR CONSTITUENTS

NAME	H	G
ZO	50.107	0.0
MM	0.066	61.4
MSF	0.060	178.1
Q1	0.034	40.0
O1	0.171	82.6
M1	0.014	267.8
K1	0.148	232.0
J1	0.007	143.9
OO1	0.070	18.0
MU2	0.003	215.9
N2	0.253	95.7
M2	1.200	111.8
L2	0.061	119.6
S2	0.408	157.2
2SM2	0.009	13.1
MO3	0.026	128.6
M3	0.003	45.9
MK3	0.017	294.5
MN4	0.034	244.0
M4	0.031	299.2
SN4	0.023	77.7
MS4	0.069	19.8
2MN6	0.018	77.7
M6	0.023	74.8
MSN6	0.008	282.1
2MS6	0.007	83.0
2SM6	0.010	250.6

Table 4a. Results of the harmonic analysis for the east-west currents at Station L Bot.

RELATED CONSTITUENTS

REL CONST.	REFERENCE CONST.	H (m/s)	G (°)
PI1	K1	0.014	37.3
P1	K1	0.074	25.0
PSI1	K1	0.009	233.0
PHI1	K1	0.015	170.3
2N2	N2	0.052	200.0
NU2	N2	0.115	219.7
T2	S2	0.053	285.8
K2	S2	0.287	284.8

MAJOR CONSTITUENTS

NAME	H	G
ZO	49.93	-
MM	0.041	104.3
MSF	0.142	352.5
Q1	0.096	179.9
O1	0.292	244.3
M1	0.033	83.2
K1	0.244	39.0
J1	0.062	78.6
OO1	0.034	198.8
MU2	0.077	172.8
N2	0.547	218.7
M2	2.888	245.8
L2	0.108	255.3
S2	1.003	285.8
2SM2	0.025	179.9
MO3	0.010	320.4
M3	0.024	237.4
MK3	0.012	201.1
MN4	0.052	129.9
M4	0.116	156.9
SN4	0.026	225.9
MS4	0.078	208.2
2MN6	0.021	359.1
M6	0.035	26.2
MSN6	0.004	330.2
2MS6	0.018	72.5
2SM6	0.002	265.0

Table 4b. Results of the harmonic analysis for the north-south currents at Station L Bot.

	anticlockwise		clockwise		semi major axis	semi minor axis	coeff rotat	major axis orientation	β
	g°	H	g°	H					
π_1	72	0.098	173	0.072	0.170	0.026	0.296	125.1°	47.4°
P1	90	0.511	160	0.375	0.886	0.136	0.301	125.0	35.2
ψ 1	-120	0.062	6	0.045	0.107	0.016	0.294	-56.9	62.7
ϕ 1	-55	0.106	-54	0.078	0.184	0.028	0.299	-54.2	0.7
2N2	-102	0.374	-30	0.281	0.655	0.093	0.280	-66.0	36.0
ν 2	-121	0.830	-10	0.617	1.447	0.212	0.287	-65.5	55.9
T2	170	0.349	67	0.297	0.647	0.052	0.159	118.3	128.3
K2	171	1.872	66	1.594	3.466	0.279	0.160	118.5	127.3
Mm	-142	1.053	-73	0.367	1.420	0.685	0.783	-107.4	34.6
Msf	139	1.426	-38	0.203	1.629	1.223	0.960	50.7	91.3
Q1	-92	0.644	-95	0.237	0.881	0.407	0.761	-93.5	178.1
O1	-129	2.102	-18	1.159	3.261	0.943	0.534	-73.6	55.6
M1	-17	0.178	175	0.239	0.418	0.061	-0.284	78.9	-83.9
K1	76	1.685	174	1.236	2.921	0.449	0.300	124.9	49.2
J1	-10	0.253	-160	0.339	0.592	0.086	-0.286	-85.1	-74.9
OO1	-87	0.405	10	0.448	0.853	0.043	-0.100	-38.3	-131.7
μ 2	-85	0.315	-43	1.519	1.835	1.204	-0.917	-63.8	-159.2
ν 2	-120	3.936	-11	2.928	6.864	1.008	0.287	-65.5	54.9
M2	-146	19.646	17	14.116	33.762	5.530	0.319	-64.4	81.7
L2	-137	1.015	-106	0.673	1.688	0.343	0.390	-121.5	15.2
S2	170	6.550	67	5.575	12.124	0.975	0.160	118.5	128.3
2SM2	-97	0.386	152	0.346	0.732	0.040	0.110	27.5	124.4
MO3	-94	0.132	85	0.319	0.451	0.187	-0.707	-4.7	-90.3
M3	-59	0.248	-47	0.190	0.438	0.058	0.259	-52.6	6.0

Table 5 (continued on second sheet)

	anticlockwise		clockwise		semi major axis	semi minor axis	coeff rotat.	major axis orien-tation	
	g	H	g	H					
MK3	-11	0.259	-166	0.221	0.480	0.038	0.156	-88.4	102.2
MN4	-119	0.083	-144	0.463	0.543	0.379	-0.937	-131.5	-12.7
M4	-33	0.409	-88	0.392	0.801	0.018	0.044	-60.9	152.6
SN4	126	0.027	-15	0.299	0.326	0.271	-0.983	55.7	-70.2
MS4	-63	0.508	-15	0.509	1.017	0.001	-0.002	-39.0	-155.6
MN6	71	0.111	59	0.099	0.210	0.012	0.118	64.8	174.2
M6	39	0.140	112	0.414	0.554	0.274	-0.795	75.3	-143.7
MSN6	28	0.196	50	0.188	0.384	0.009	0.046	38.7	10.9
2MS6	-65	0.241	-156	0.303	0.544	0.062	-0.226	-110.6	-45.1
2SM6	174	0.212	-43	0.303	0.515	0.091	-0.344	65.4	-108.6

Table 5. (continued) Ellipse analysis of 25 days current meter data at LTOP. Current meter 20 m below the surface. Total depth is 70 m

g is phase relative to $t=0$ and H is amplitude in cm per second. β is phase angle between $t=0$ and the time of flow along the major axis.

Constituent	Stations	Observations	Theoretical
M_2	G	0.14	0.05
	H	0.23	0.04
S_2	G	0.16	0.05
	H	0.20	0.04
M_2	K	0.09	0.03
	L	0.22	0.03
S_2	J	0.32	0.01
	K	0.15	0.03
	L	0.19	0.03
	J	0.27	0.02

Table 6. Comparison between the ratios of minor axis to major axes of the current ellipses from observations and theoretical Kelvin propagation with rectilinear bathymetry.

	Station				
	K	L	J	G	H
Observation a(station) : a(i)	1.00	0.92	0.70	1.00	0.70
Theoretical a(station) : a(i)	1.00	0.86	0.57	1.00	0.85
Observation {station : {coast		0.80	0.54		0.76
Theoretical {station : {coast		0.74	0.48		0.72

Table 7. Comparison between observed and theoretical current and elevation ratios along two sections KLJ and GH, at the M_2 frequency. a is the amplitude of the currents along the major axis of the ellipse; i means K for the line KLJ, and G for the line GH.

Station	Depth (m)	theoretical ratio (a)	theoretical ratio (b)	Observed ratio
H top				3.58
H bottom	77			4.19
H averaged		2.80	2.61	3.86
J top				3.59
J bottom	75			3.77
J averaged		2.77	2.21	3.68
L top				3.79
L bottom	70			4.24
L averaged		2.67	2.17	4.00

Table 8. Comparison between the ratios of maximum elevation/maximum current for the observed results and the theoretical results for (a) a Kelvin wave with a flat bottom and linear coast $(D/g)^{\frac{1}{2}}$ and (b) the results for a Kelvin wave with bathymetric contours parallel to a straight coastline.

	Wp	Qp (°)	Wnp	Qnp (°)	Major axis direction (°)	Semi major axis
E top	4.9	-61	2.1	59	-66	5.0
H top	3.4	-63	1.1	69	-66	3.5
H bottom	2.9	-66	1.1	69	-70	3.0
J top	1.8	-93	1.7	55	-109	2.4
J bottom	1.6	-86	1.9	55	-109	2.3
L top	3.4	-63	0.7	58	-64	3.4
L bottom	2.9	-68	1.2	66	-73	3.0
P top	3.1	-90	1.7	66	-95	3.5
P bottom	2.7	-88	2.0	58	-99	3.2
Inner Dowsing	5.5	-82	4.5	66		
Shell Esso	6.2	-70	4.8	-97		
Zo	6.0	-44	2.8	90		

Table 9a. Decomposition of observed M_2 tidal elevations and currents into progressive and non-progressive parts.
W is the current amplitude in decimetres per second and Q is the direction of flow.

	Wp	Qp	Wnp	Qnp	Major axis direction	Semi major axis
E (top)	1.7	-60	0.9	61	111	1.8
H top	1.3	-62	0.4	81	116	1.3
H Bot	1.1	-64	0.5	81	111	1.2
J top	0.7	-94	0.6	62	75	0.9
J Bot	0.6	-86	0.6	57	72	0.8
L top	1.2	-61	1.0	45	119	1.2
L Bot	1.0	-68	0.5	65	106	1.0
P top	1.1	-92	0.6	65	-97	1.2
P Bot	0.9	-89	0.7	57	-101	1.1
Inner Dowsing	1.8	-88	2.9	33		

Table 9b. As for Table 9a, and the S_2 tidal constituent.

	Wp	Qp	Wnp	Qnp	Major axis direction	Semi major axis
E top	0.4	-46	0.3	107	-55	0.5
H top	0.3	-60	0.2	89	-71	0.3
H Bot	0.3	-61	0.2	87	-70	0.3
J top	0.2	-68	0.2	73	-90	0.2
J Bot	0.2	-65	0.2	78	-84	0.2
L Top	0.3	-54	0.1	73	-55	0.3
L Bot	0.3	-58	0.1	98	-59	0.3
P top	0.2	-81	0.1	81	-96	0.3
P Bot	0.3	-79	0.1	77	-81	0.3
Inner Dowsing	0.2	-100	0.4	93		

Table 9c. As for Table 9a, and the K1 tidal constituent.

	Wp	Qp	Wnp	Qnp	Major axis direction	Semi major axis
E (top)	0.5	-49	0.3	96	-60	0.5
H top	0.3	-62	0.2	92	-71	0.4
H Bot	0.3	-63	0.2	91	-70	0.3
J top	0.2	-68	0.2	70	-94	0.3
J Bot	0.2	-66	0.2	75	-88	0.3
L top	0.3	-65	0.2	77	-74	0.3
L Bot	0.3	-58	0.1	90	-60	0.3
P top	0.3	-88	0.2	83	-90	0.3
P Bot	0.3	-78	0.1	83	-81	0.3
Inner Dowsing	0.2	-85	0.4	89		

Table 9d. As for Table 9a, and the O1 tidal constituent.

Station	M2		S2		K1		O1	
	c	e	c	e	c	e	c	e
E	4.35	4.83	5.53	6.20	3.59	5.85	5.24	7.74
H top	3.35	3.76	4.60	5.10	2.49	4.79	4.23	6.81
bottom	3.21		4.40		2.66		4.52	
J top	1.73	3.21	3.07	4.47	1.26	4.52	3.01	6.81
bottom	1.45		2.80		1.53		3.23	
L top	2.83	3.04	4.27	4.33	3.32	3.72	4.02	5.95
bottom	2.45		3.70		2.86		4.95	
P top	1.04	1.97	2.33	3.23	0.86	2.06	2.65	4.88
bottom	0.79		2.07		1.13		3.08	

Table 10. Observed time lags in hours for the maximum elevations (e) (high tide) and for the maximum current (c) (major axis flow) relative to Greenwich Meridian phases, for the principal harmonic tidal constituents.

Station	anticlockwise		clockwise		semi major axis	semi minor axis	coeff rotat	major axis orientation
	g°	H	g°	H				
E	174	32.7	73	13.4	46.1	19.3	0.713	123°
F	-169	27.7	38	18.4	46.0	9.3	0.388	-65
G	-148	25.2	27	17.1	42.3	8.1	0.371	-60
H	-154	22.8	22	13.0	35.8	9.9	0.512	-66
I	-141	22.6	22	14.2	36.8	8.4	0.436	-59
J	-150	16.3	-71	8.0	24.3	8.3	0.613	-110
K	-139	20.4	-2	13.5	33.8	6.9	0.390	-70
L	-140	20.1	1	10.8	30.8	9.3	0.554	-69
M	-131	21.2	-9	12.7	33.9	8.5	0.472	-70
N	-118	20.9	-12	11.9	32.8	9.0	0.511	-65
P	-122	19.4	-67	10.7	30.1	8.7	0.532	-95

Table 11a. Numerical model results for current ellipses at M_2 tidal frequency.

Station	ant-clockwise		clockwise		semi major axis	semi minor axis	coefficient of rotation	Major axis orientation
	g°	H	g°	H				
E	168	34.0	60	16.0	49.9	18.0	0.638	114°
	-174	28.7	24	17.0	45.6	11.7	0.481	-75
G	-150	26.3	24	20.0	46.2	6.3	0.268	-63
H top	-163	21.5	30	13.6	35.1	7.8	0.425	-66
H bottom	-163	16.8	22	11.1	29.9	7.8	0.486	-70
I top	-148	20.9	27	16.8	37.7	4.1	0.214	-60
J top	-157	15.5	-60	8.7	24.1	6.8	0.524	-108
J bottom	-151	15.2	-68	7.5	23.0	8.0	0.623	-109
K	-147	17.8	-12	14.8	32.6	3.0	0.182	-79
L top	-146	20.0	17	14.1	33.8	5.5	0.319	-64
M	-129	21.8	1	20.7	42.5	1.1	0.051	-64
N	-126	19.7	-21	10.9	30.6	8.8	0.532	-73
P top	-125	23.5	-65	14.4	35.0	6.1	0.339	-95
P bottom	-122	20.5	-77	11.3	31.7	9.2	0.536	-99

Table 11b. Observed current ellipses at the M_2 tidal frequency.

g is phase relative to $t=0$ and H is amplitude in cm per second.

Stations	P	U	L	S	H	Q
Observed amplitude cm	120.6	154.7	128.0	159.7	125.7	164.8
Model amplitude cm	108.2	141.3	113.4	148.3	116.5	152.2
Observed phase (°)	57.4	59.2	87.7	88.7	109.2	103.8
Model phase (°)	56.1	59.1	86.8	85.2	108.6	106.6

Table 12. Comparisons for M_2 between the elevations (amplitude and phase) from observations and from the numerical model output.

Stations	P	L	J	H	E
Observed amplitudes cm	3.0	1.7	1.6	2.6	2.1
Model amplitudes cm	2.6	2.1	1.1	2.2	2.0
Observed phase	175.9	104.0	90.1	83.0	118.0
Model phase	154.3	120.3	96.1	101.3	141.7

Table 13. Comparison for M_4 between the elevations from observations and from the numerical model output.

Station	semi major axis	semi minor axis	coeff rotat	major axis orientation
E	1.45	0.45	0.56	163°
F	0.60	0.20	0.59	4
G	0.50	0.26	-0.82	-135
H	0.56	0.31	-0.86	-147
I	0.50	0.40	-0.98	-91
J	1.00	0.65	-0.91	-1
K	0.53	0.24	-0.75	-68
L	0.67	0.51	-0.96	-45
M	0.72	0.30	-0.70	-52
N	0.95	0.30	-0.58	-35
P	0.92	0.46	-0.80	-14

Table 14a. Numerical model results for currents ellipses at M4 tidal frequency. Speeds are cm/sec.

Station	semi major axis	semi minor axis	coefficient of rotation	major axis orientation
E	2.0	0.6	0.55	113.0
F	1.0	0.5	0.81	-127.0
G	0.4	0.2	0.81	-5.1
H top	0.4	0.1	-0.45	24.0
H bottom	0.5	0.3	-0.89	-88.0
I top	1.5	0.2	0.31	-122.0
I bottom	0.7	0.2	-0.58	-99.0
J top	0.6	0.4	-0.90	-107.0
J bottom	0.8	0.3	-0.68	-109.0
K	0.4	0.2	0.84	-47.0
L top	0.8	0.0	0.04	-61.0
L bottom	1.2	0.2	-0.30	-67.0
M	0.9	0.1	0.27	-58.0
N top	1.6	0.5	-0.58	-49.0
N bottom	1.5	0.4	-0.56	-33.0
P top	1.4	0.7	-0.79	-23.0
P bottom	1.1	0.4	-0.56	-37.0

Table 14b. Observed current ellipses at the M_4 tidal frequency.
Speeds are cm/sec.

Station	M2	S2	K1	O1
H	0.14	0.20	-0.17	-0.29
I	0.20	0.28	-0.98	-1.03
J	0.28	0.27	-0.27	-0.22
L	0.38	0.57	-0.54	-0.93
P	0.35	0.26	-0.27	-0.43
N	0.26	0.11	-0.29	-0.09

Table 15. Time difference equivalent of the phase difference and the bottom current meter tidal constituents. Times are in hours.

Positive values mean that the maximum current event happens earlier at the bottom station than at the top.

Station	M_2		S_2		K_1		O_1	
	a	c	a	c	a	c	a	c
H	0	8	-2	11	3	-3	2	-3
J	-6	8	-5	10	-2	-11	-2	-10
L	-3	-2	-5	31	-2	11	0	-27
P	-3	12	-4	-25	-10	-50	-3	-14
I	-4	14	-4	22	0	-29	-10	-20
N	-8	7	-12	-5	-14	-22	-13	-16

Table 16. Phase lag between the top and the bottom current metres for the anti clockwise (a) and clockwise (c), parts of the current .

The orientation of the angles is positive anti clockwise.

The angles are given in degrees.

	M2		S2		K1		O1	
Station	a	c	a	c	a	c	a	c
H	0	+0.28	-0.07	+0.37	0.20	-0.20	0.14	-0.22
J	-0.21	+0.28	-0.17	+0.33	-0.13	-0.73	-0.14	-0.72
L	-0.10	-0.70	-0.17	+1.03	-0.13	+0.73	0	-1.94
P	-0.10	+0.41	-0.13	-0.83	-0.66	-3.32	-0.22	-1.00
I	-0.14	+0.48	-0.13	+0.73	0	-1.93	-0.72	-1.44
N	-0.28	+0.24	-0.40	+0.17	-0.93	-1.46	-0.93	-1.15

Table 17. Times in hours, equivalent to the phase lags shown in Table 16.

	Box SLPU	Box QHLS	Box QHLPU
input water flux	0.310	0.360	0.403
output water flux	0.267	0.402	0.402
balance	0.044	-0.042	-0.001

Table 18a. Water flux budget with linear interpolation along every boundary.
Units are 10^5 m^3 / sec

	Box SLPU	Box QHLS	Box QHLPU
input water flux	0.310	0.407	0.403
output water flux	0.314	0.402	0.402
balance	-0.004	0.005	-0.001

Table 18b. Water flux budget with Kelvin wave shaped interpolation for SKL and linear interpolation for other boundaries.

The box QHLPU has the same results in both Tables because SKL is not a boundary for this box.

	Box SLPU	Box QHLS	Box QHLPU
energy influx	0.92	1.24	1.26
energy outflux	0.90	1.15	1.15
balance	0.02	0.09	0.11

Table 19a. Energy flux Budget for different boxes with the linear approximations.
Units are 10^{10} Watts.

	Box SLPU	Box QHLS	Box QHLPU
energy influx	0.92	1.35	1.26
energy outflux	1.01	1.15	1.15
balance	-0.09	0.20	0.11

Table 19b. Energy flux budget with the linear approximations except for SKL where a Kelvin Wave shape is adopted.

	Box SLPU	Box QHLS
linear interpolation every-where with real depth	0.02	0.09
Kelvin wave shape for SKL with real depth	-0.09	0.20
linear interpolation every-where with modified depths for SKL	0.05	0.06

Table 20. Comparisons of the results of energy fluxes for the areas SLPU and QHLS computed by different methods.

Units are 10^{10} Watts.

	Natural configuration		Numerical Model	
Section	length	orientation	length	orientation
UNP	37.6	-57^{o}	40	-45^{o}
SKL	34.5	-60.5	35.3	-54
QGH	34.7	-57	40	-48
PL	62.5	+22	66	+22
LH	42.2	+42	39	+44

Table 21. Comparisons between the natural and numerical model representations of the box boundaries. Lengths are in nautical miles.

	minimum with I_1^{ab}	maximum with I_2^{ab}	estimate with I_3^{ab}	results with rectilinear currents only I_4^{ab}
Area	0.0272	0.0294	0.0279	0.0268
Area	0.0441	0.0454	0.0444	0.0440
Total area	0.0713	0.0748	0.0723	0.0708

Table 22a. Low and upper bounds and estimations of the energy dissipation (K = 0.0025)

Units are 10^{10} Watts

	Term due to $a^3\lvert\cos\vartheta\rvert^3$	$a^2 b\cos^2\vartheta\lvert\sin\vartheta\rvert$	$a\,b^2\lvert\cos\vartheta\rvert\sin^2\vartheta$	$b^3\lvert\sin\vartheta\rvert^3$
Area	26.8	2.1	0.4	0.14
Area	44.0	1.2	0.1	0.03
Total area	70.8	3.3	0.5	0.17

Table 22b. Influence of various uses of the small axis b in the calculations of the dissipation.

Units are 10^{7} Watts

Triangular Area	De	Dr
MNP	0.500	0.475
MPL	0.691	0.662
MLK	0.479	0.475
IKL	0.265	0.250
ILH	0.434	0.400
IHG	0.422	0.400
MNu	0.415	0.407
Mut	0.380	0.379
KMt	0.520	0.519
Kts	0.629	0.625
IKs	0.310	0.306
Isr	0.710	0.706
GIr	0.795	0.782
Grq	0.678	0.675

Table 23. Summary of energy dissipated by bottom friction (K = 0.0025) in triangular areas. Dr are values estimated by rectilinear approximation of the observed ellipses at the corners. and De are values estimated by taking into account the amplitude of the minor axis.

Units are 10^{8} Watts.

	Dissipation from observations	Dissipation from model
Area QHLS	0.036	0.032
Area SLPU	0.036	0.035
Total area	0.072	0.067

Table 24. Estimated dissipation comparisons with a quadratic law (K = 0.0025)

Units are 10^{10} Watts

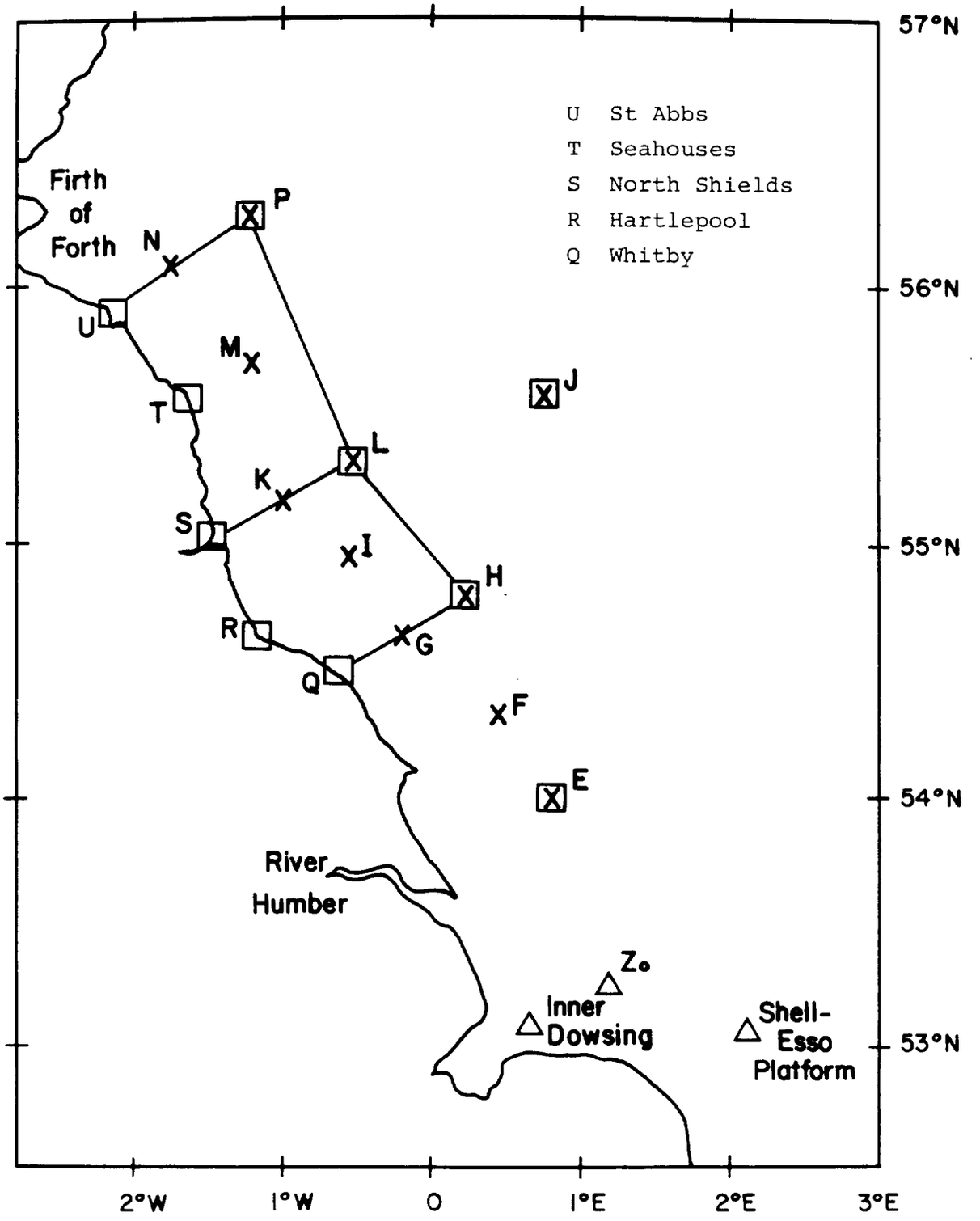

Figure 1. Area of the experiment and station positions.

× position where current has been measured.
□ position where elevation has been measured.
△ positions of previous measurements.

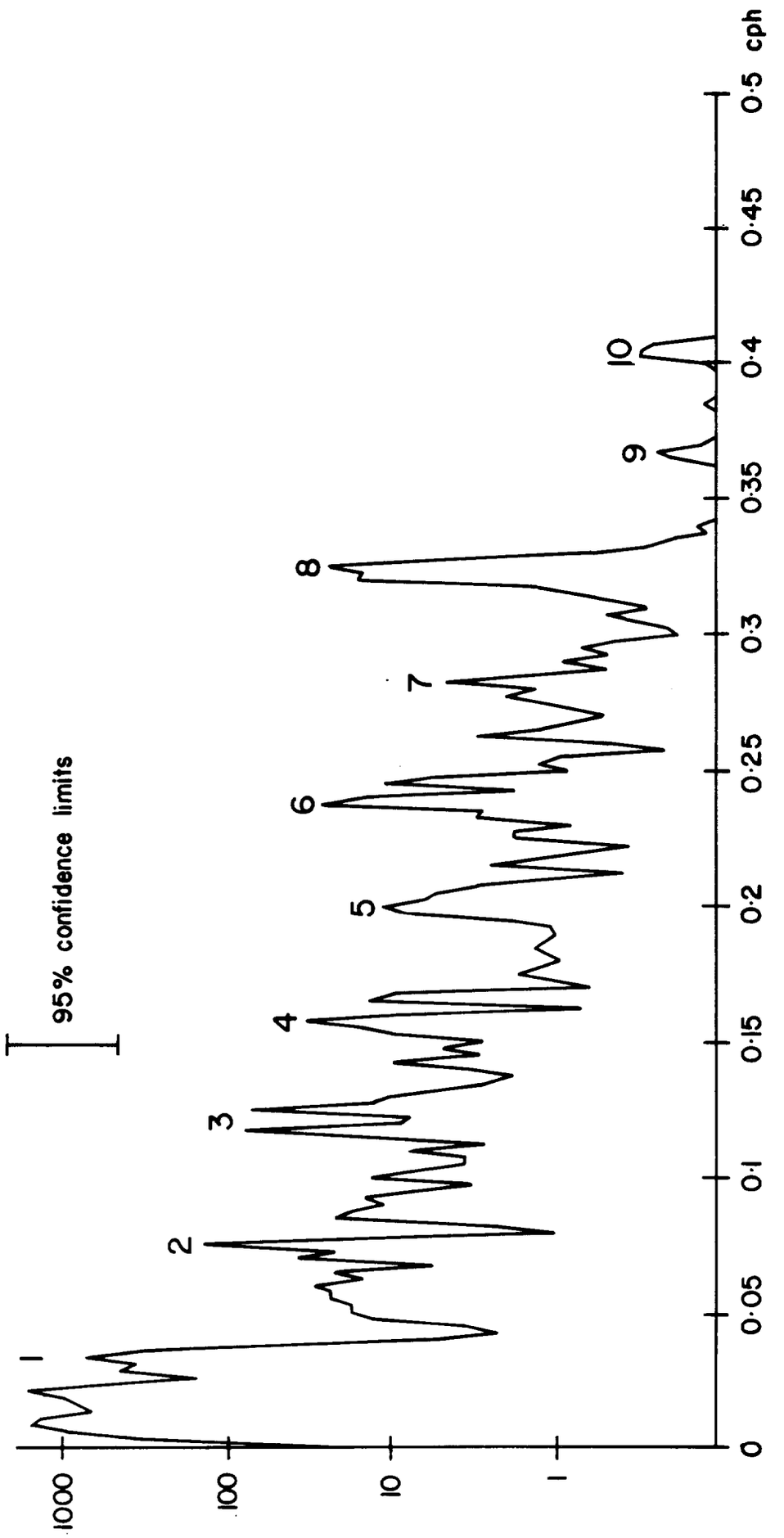

Figure 2. Relative energy spectrum of the residuals from the bottom pressure data for station L bottom. Numbers refer to the approximate positions of tidal bands.

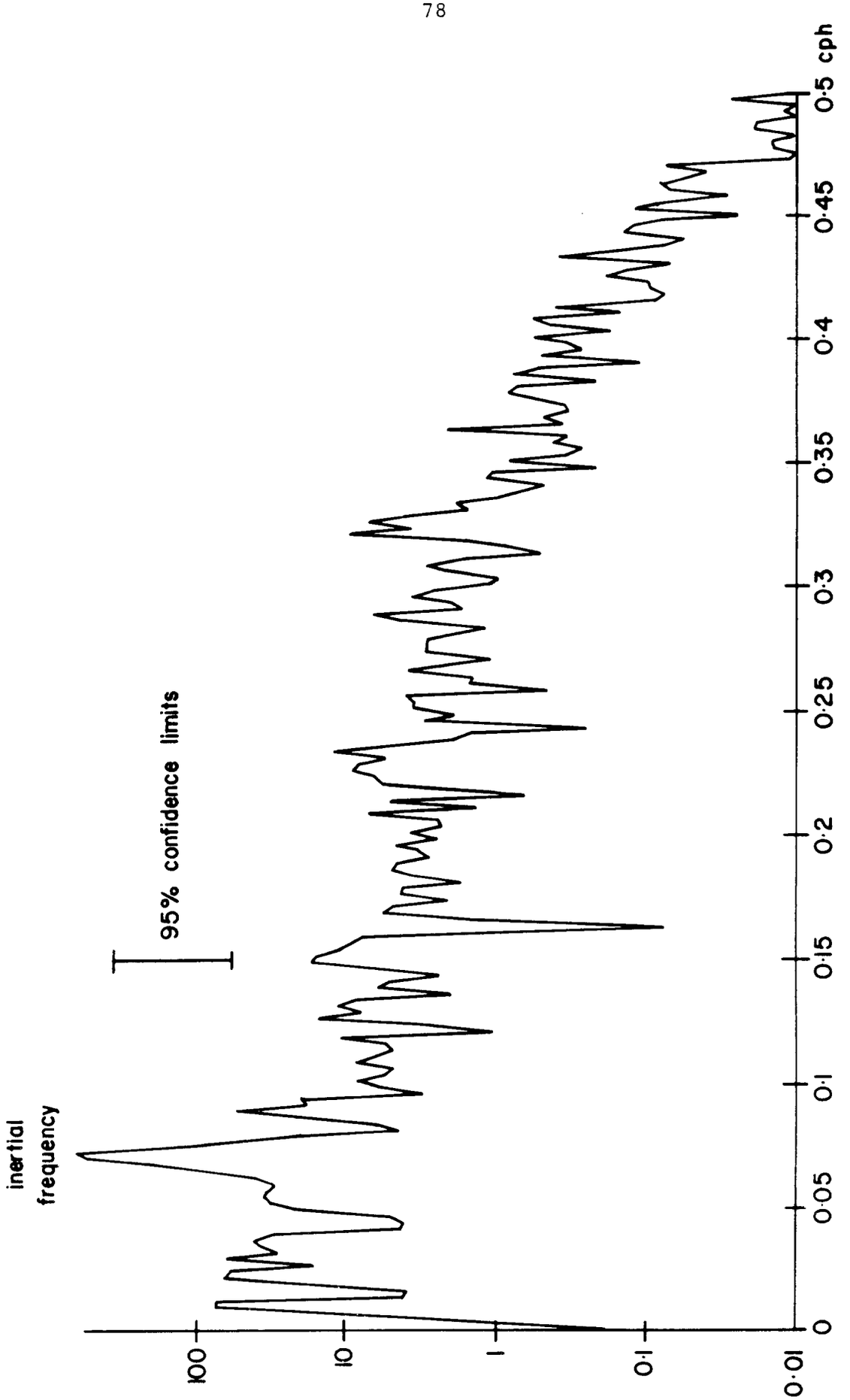

Figure 3a. Relative energy spectrum of the residuals from the u current for station L bottom.

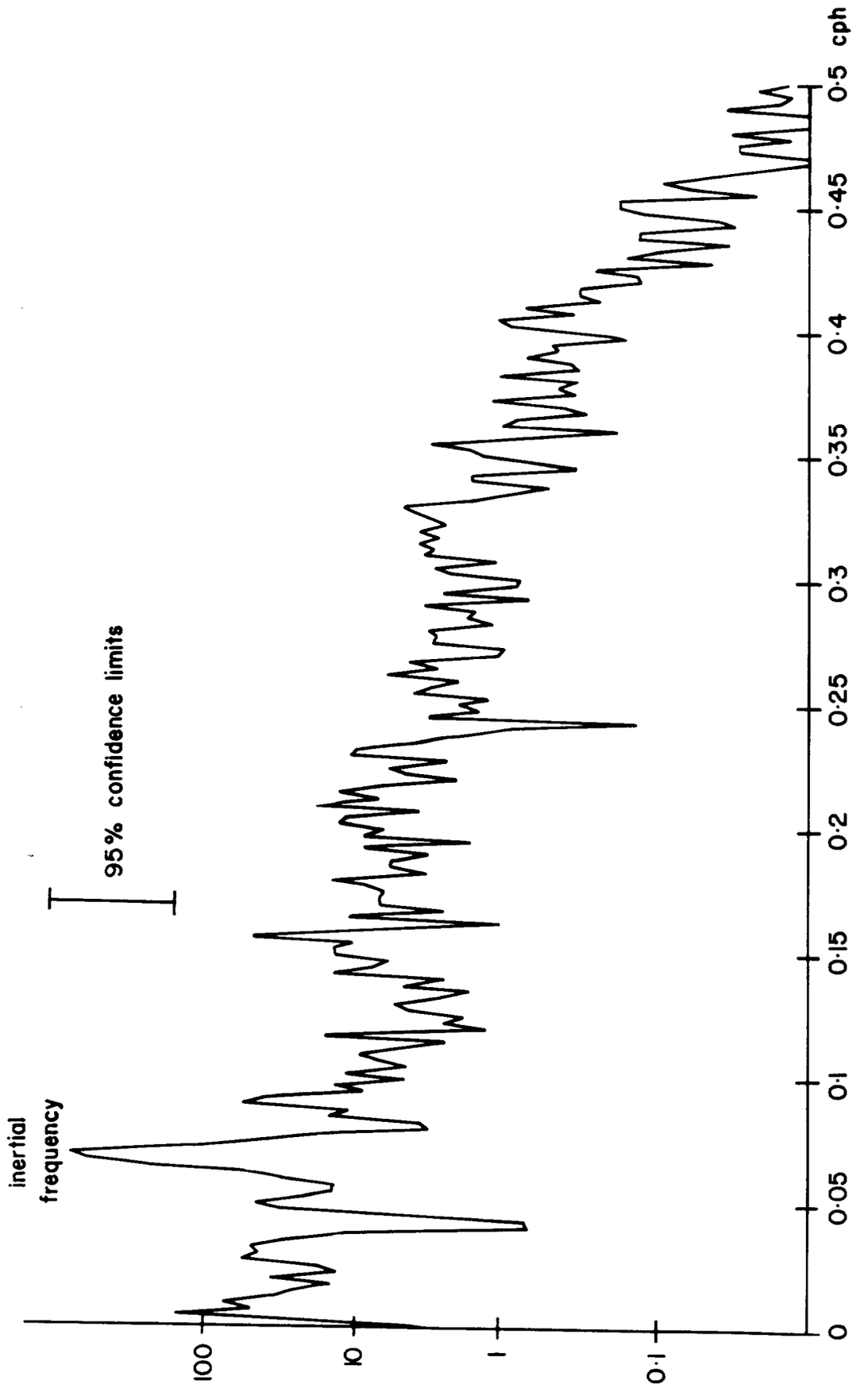

Figure 3b. Relative energy spectrum of the residuals from the V current for station L bottom.

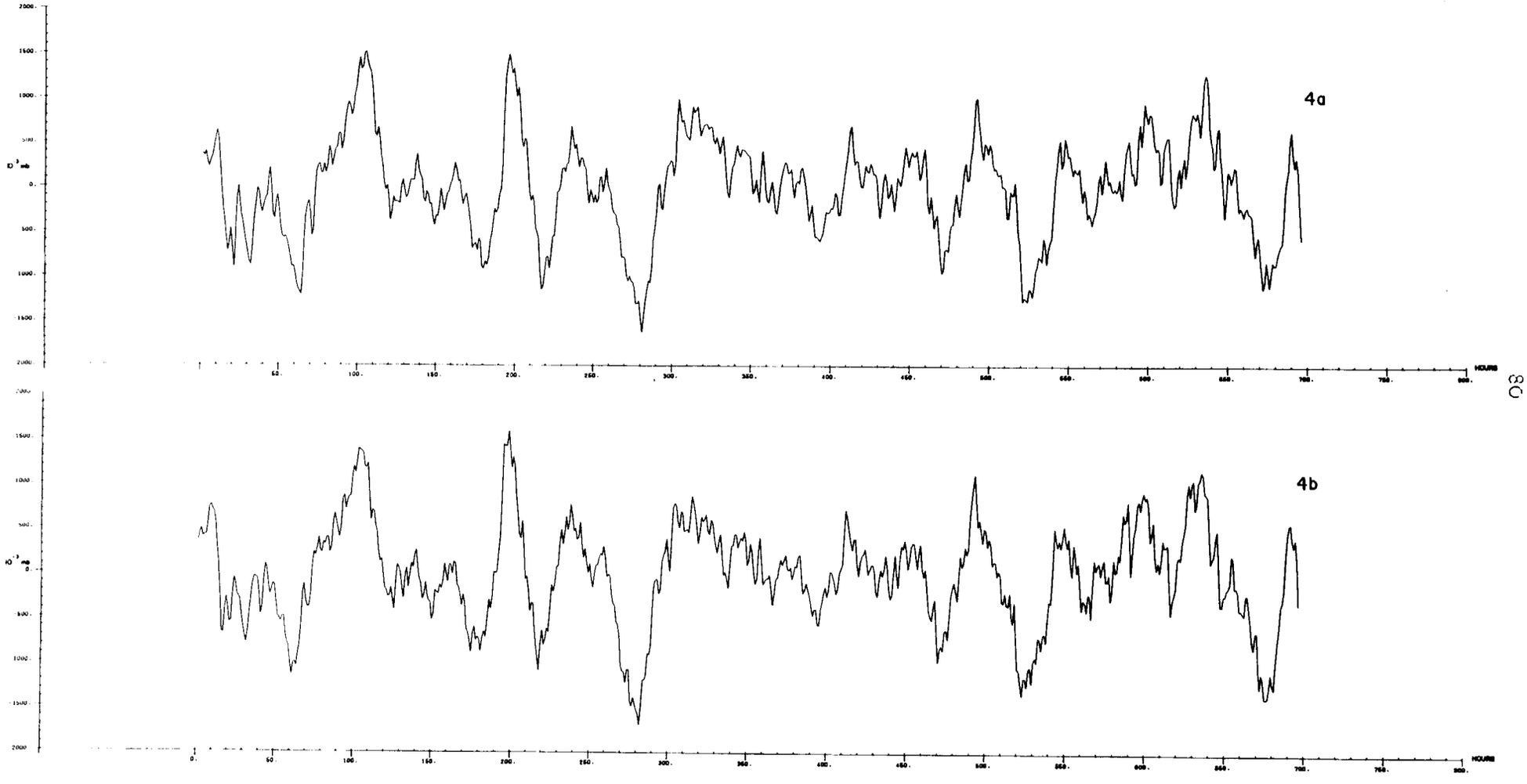

Figure 4a. Station L bottom pressure residuals

Figure 4b. Station H bottom pressure residuals

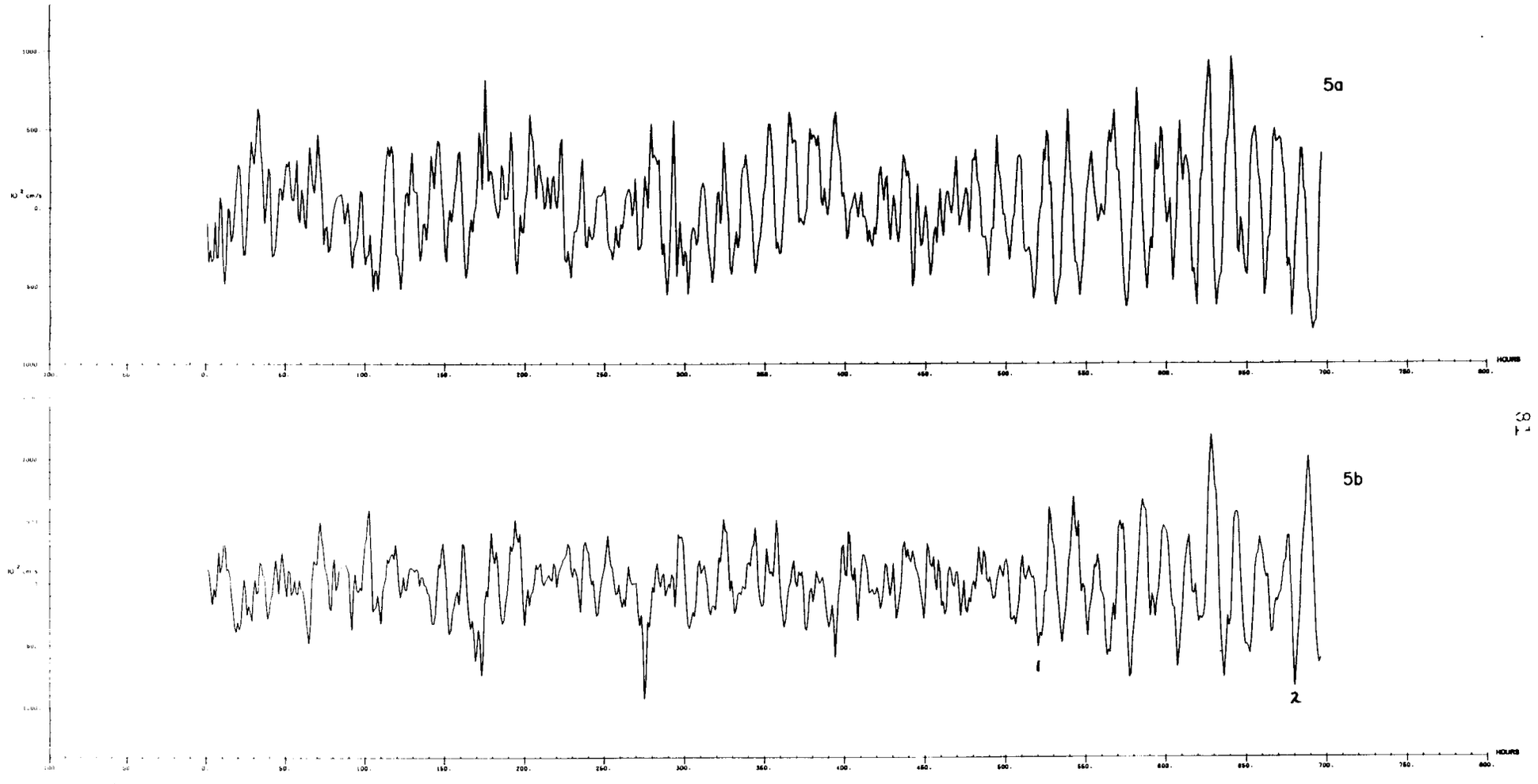

Figure 5a. Station L bottom current meter north residual

Figure 5b. Station L bottom current meter east residual

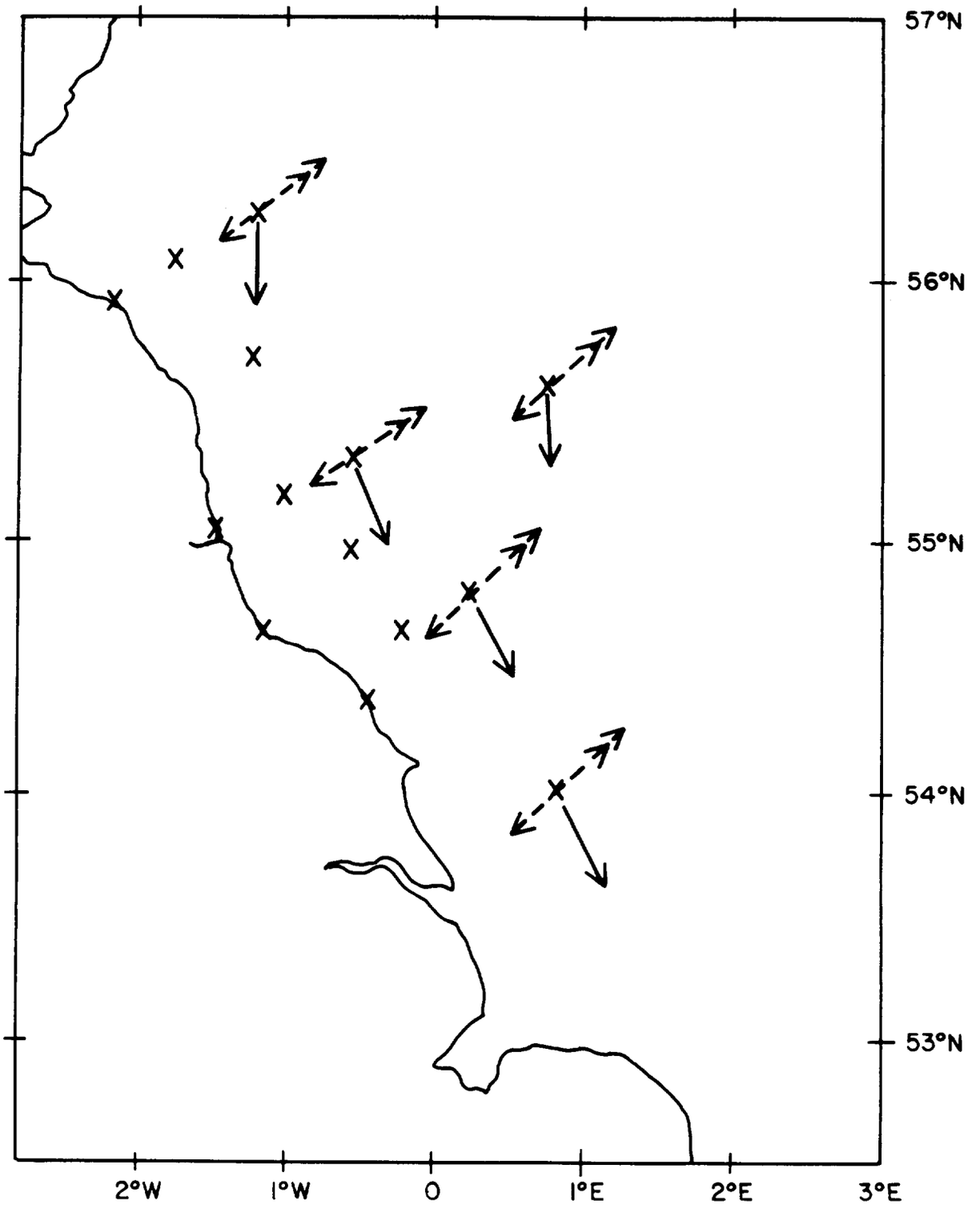

Figure 6. Decomposition of observations into a progressive wave ⟶
and a non-progressive wave — — — →
The arrows are not to scale. The double arrow gives the direction of flow from the non-progressive part of the falling tide.

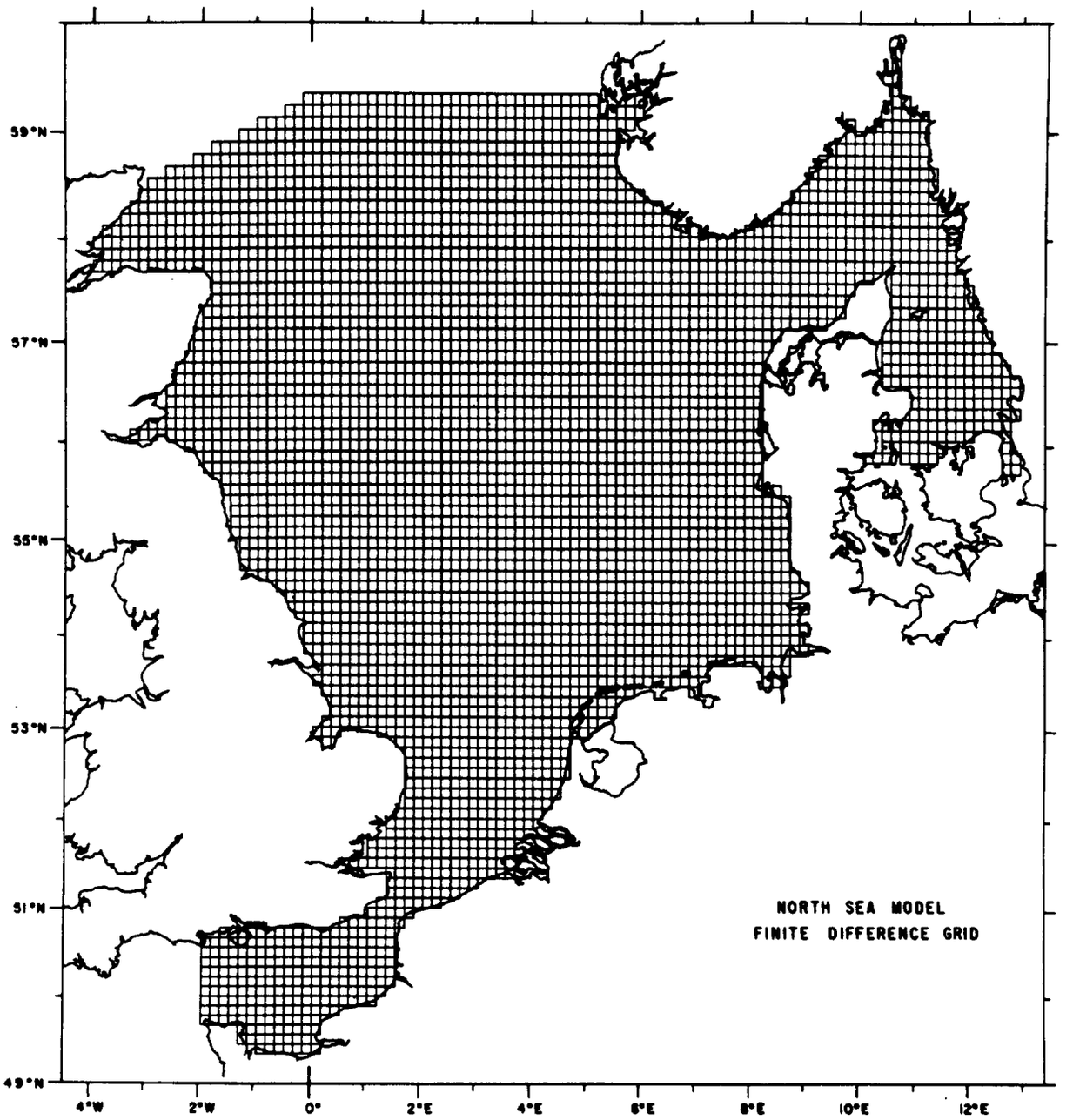

Figure 7. Computational grid for Davies' numerical model.

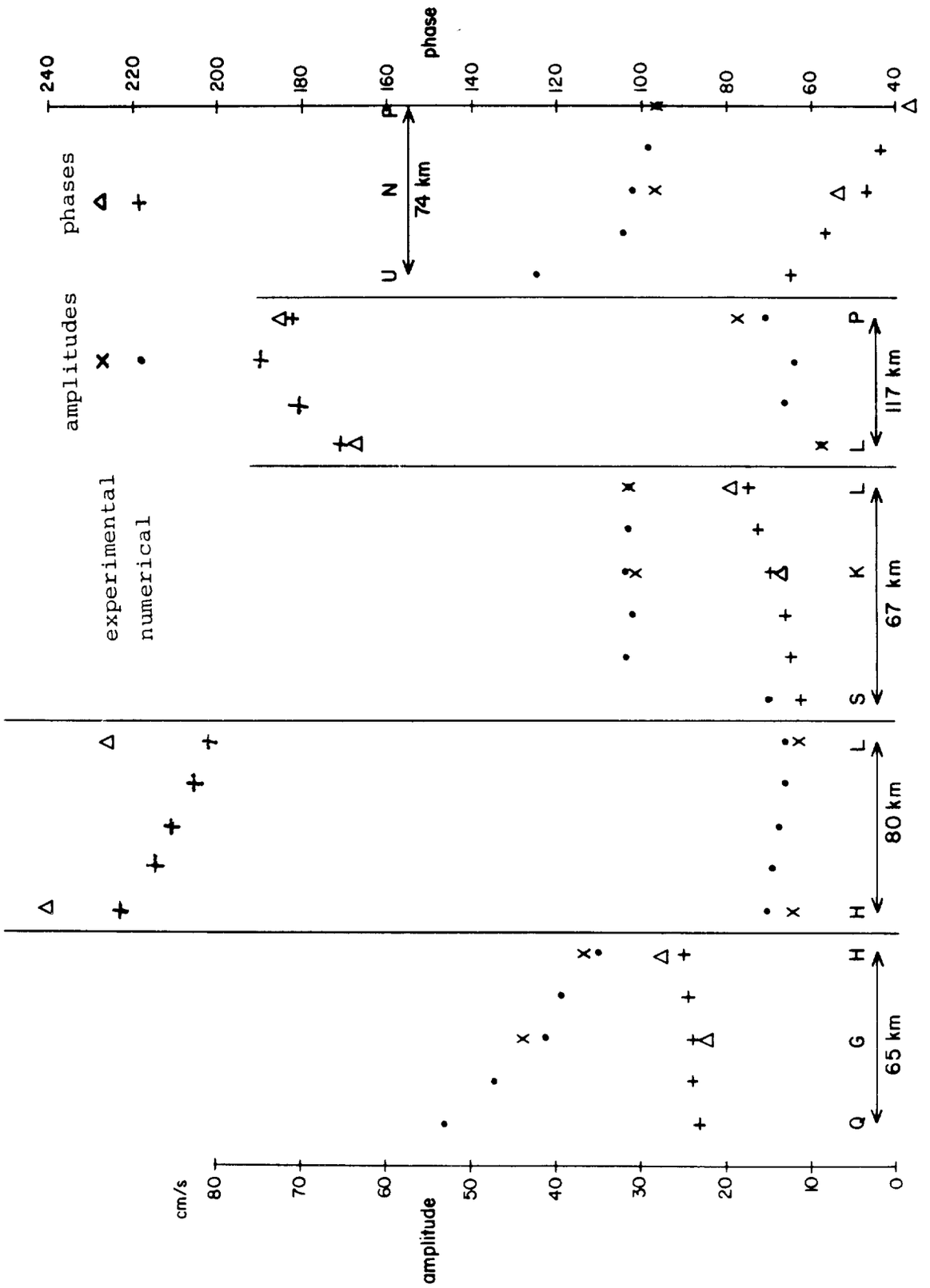

Figure 8. Comparisons between observed and numerical M2 amplitudes and phases for currents normal to box boundaries.

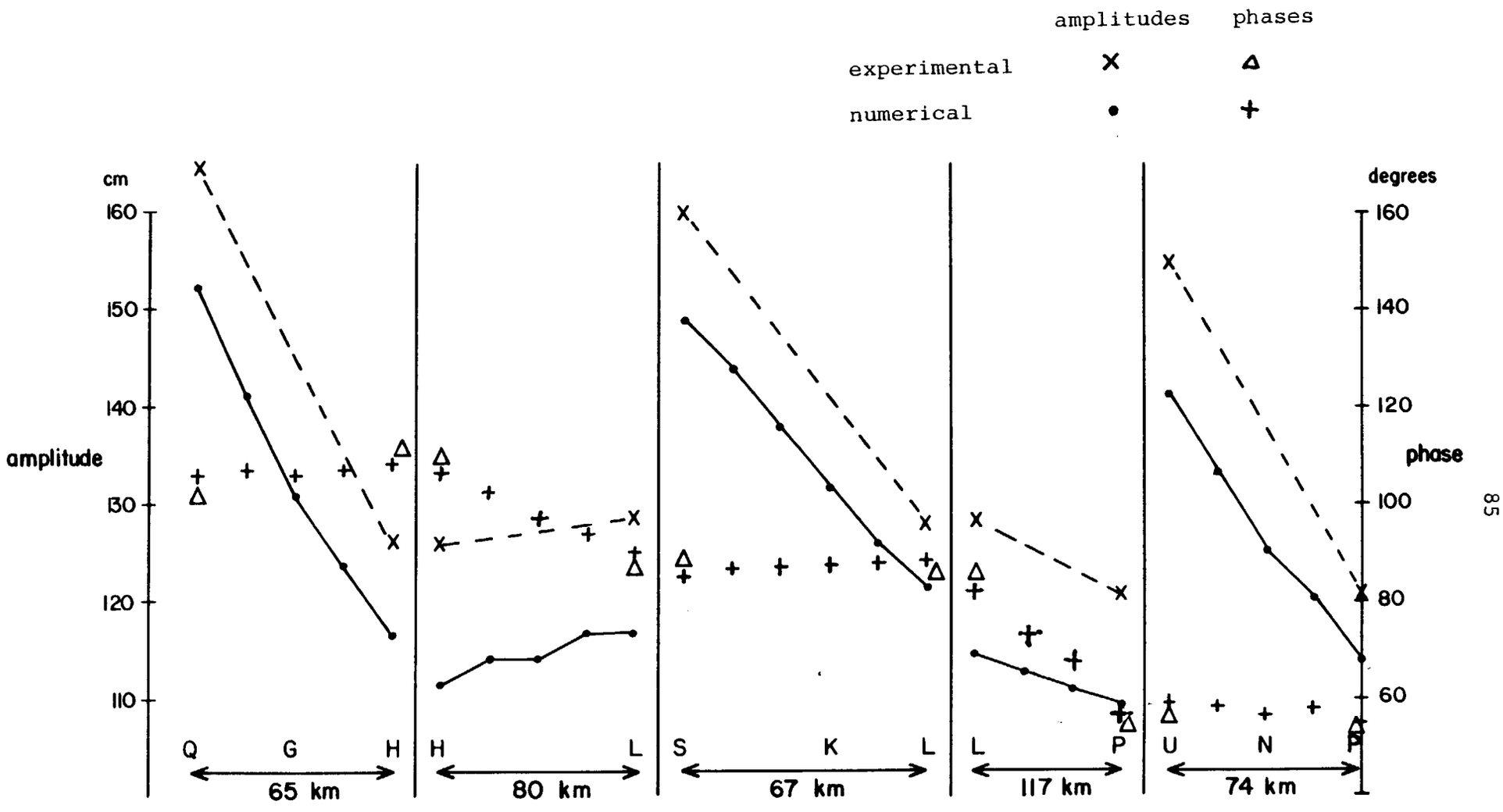

Figure 9. Comparison between observed and numerical M2 phases and amplitudes for elevations along box boundaries.

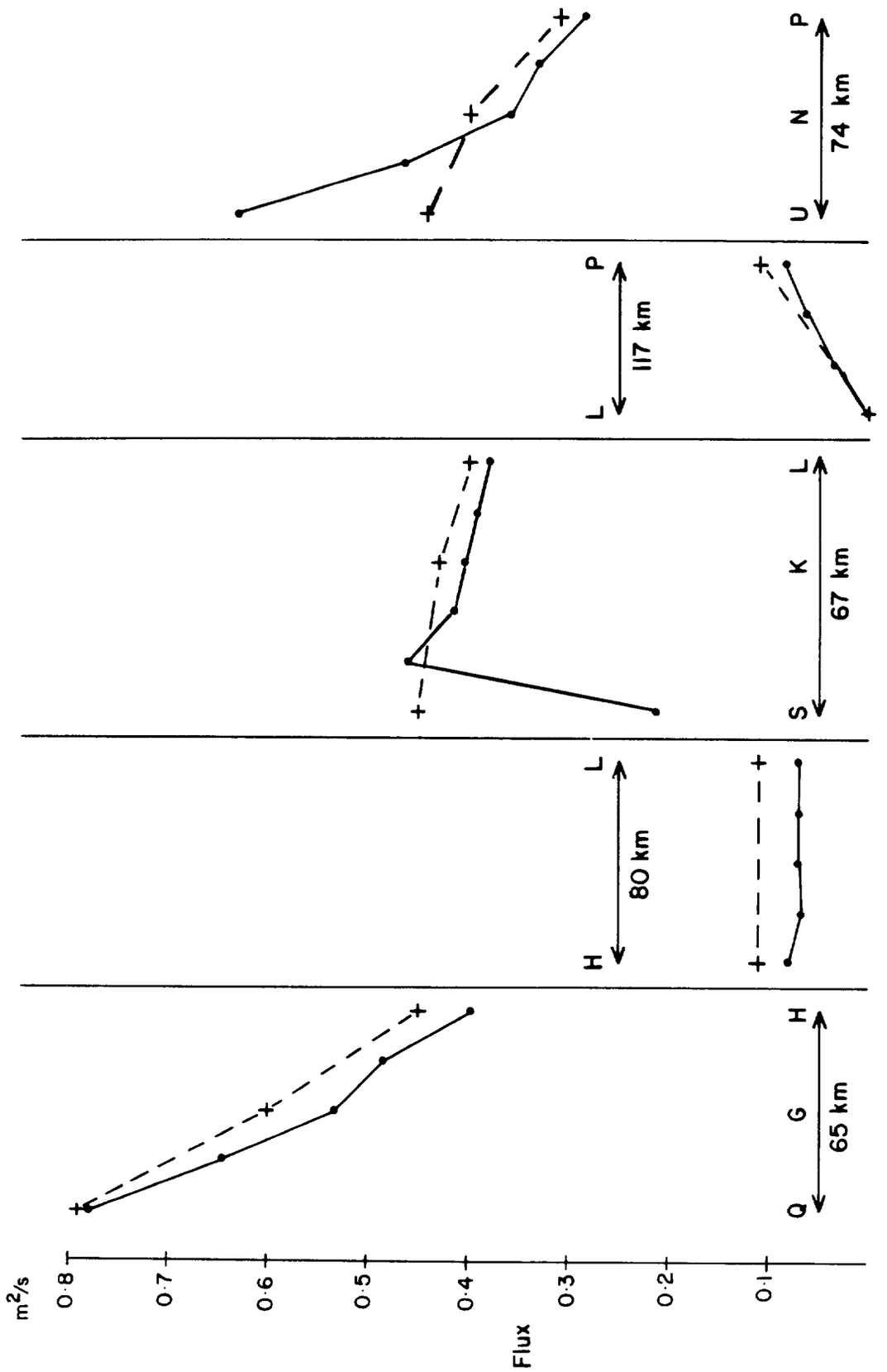

Figure 10. Comparison of estimated observed water flux and numerical model computed water flux per meter of box boundary, over a tidal period.

+ — — + experimental extrapolated water flux

• ——— • numerical model water flux

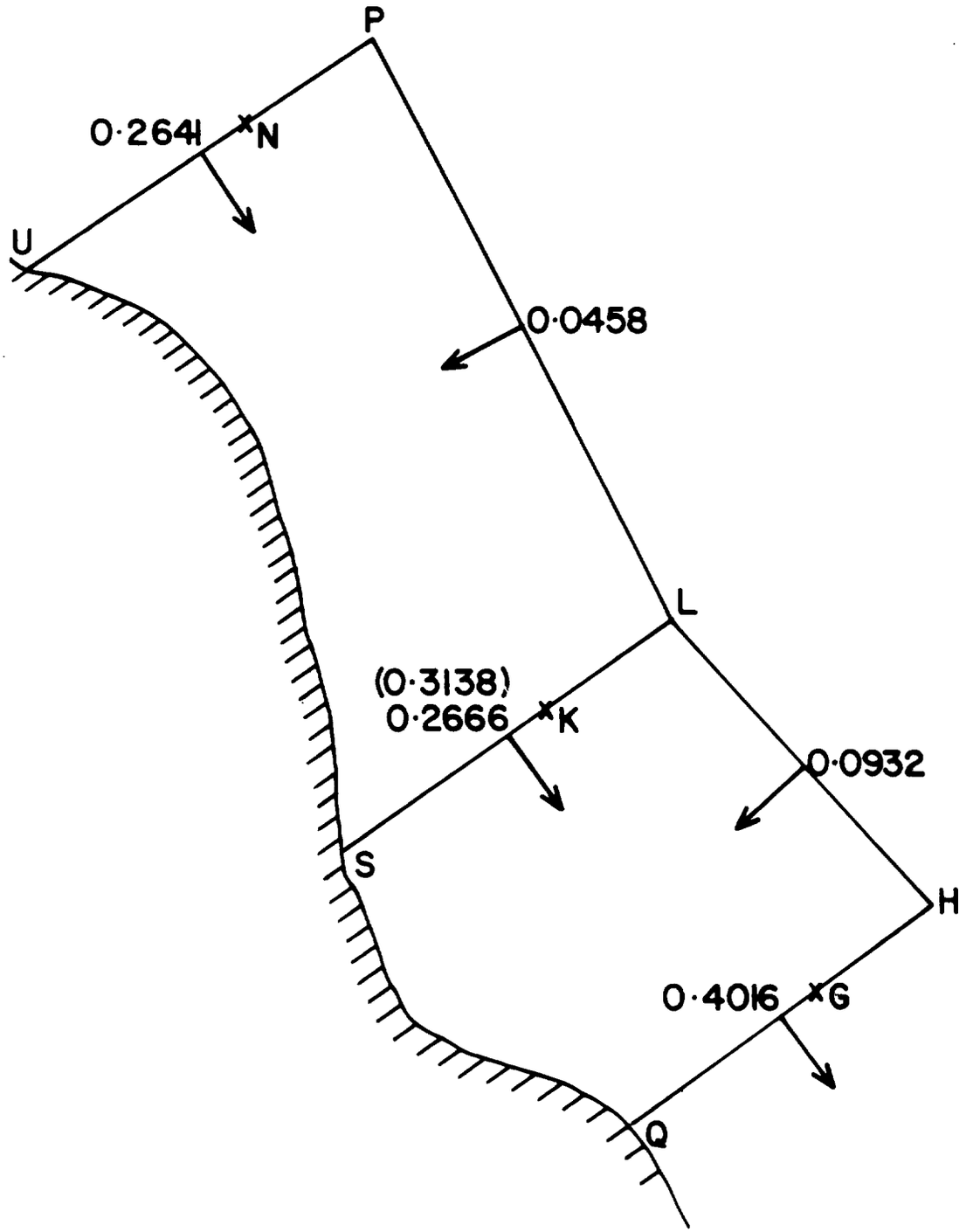

Figure 11. Water flux from observed data over a tidal cycle for M2. Units are 10^5 m^3/s.

All the fluxes are estimated by linear interpolation except (0.3138) which is the flux through SKL estimated by using an approximation from a Kelvin wave profile.

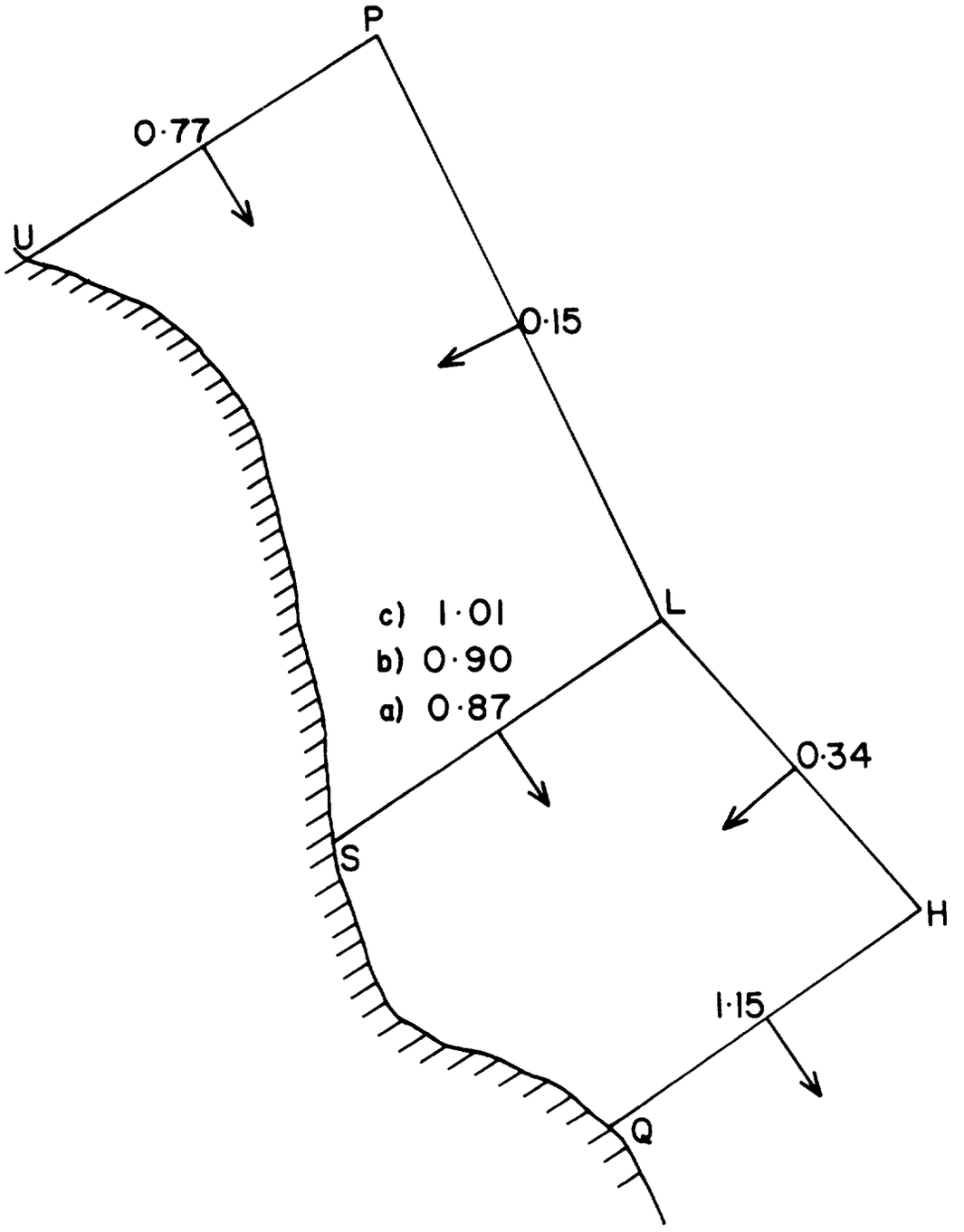

a) linear interpolation smooth profile

b) linear interpolation

c) Kelvin wave interpolation

Figure 12. Energy flux from observed data (NSt) for M2 over one tidal period. Units are 10^{10} Watts.

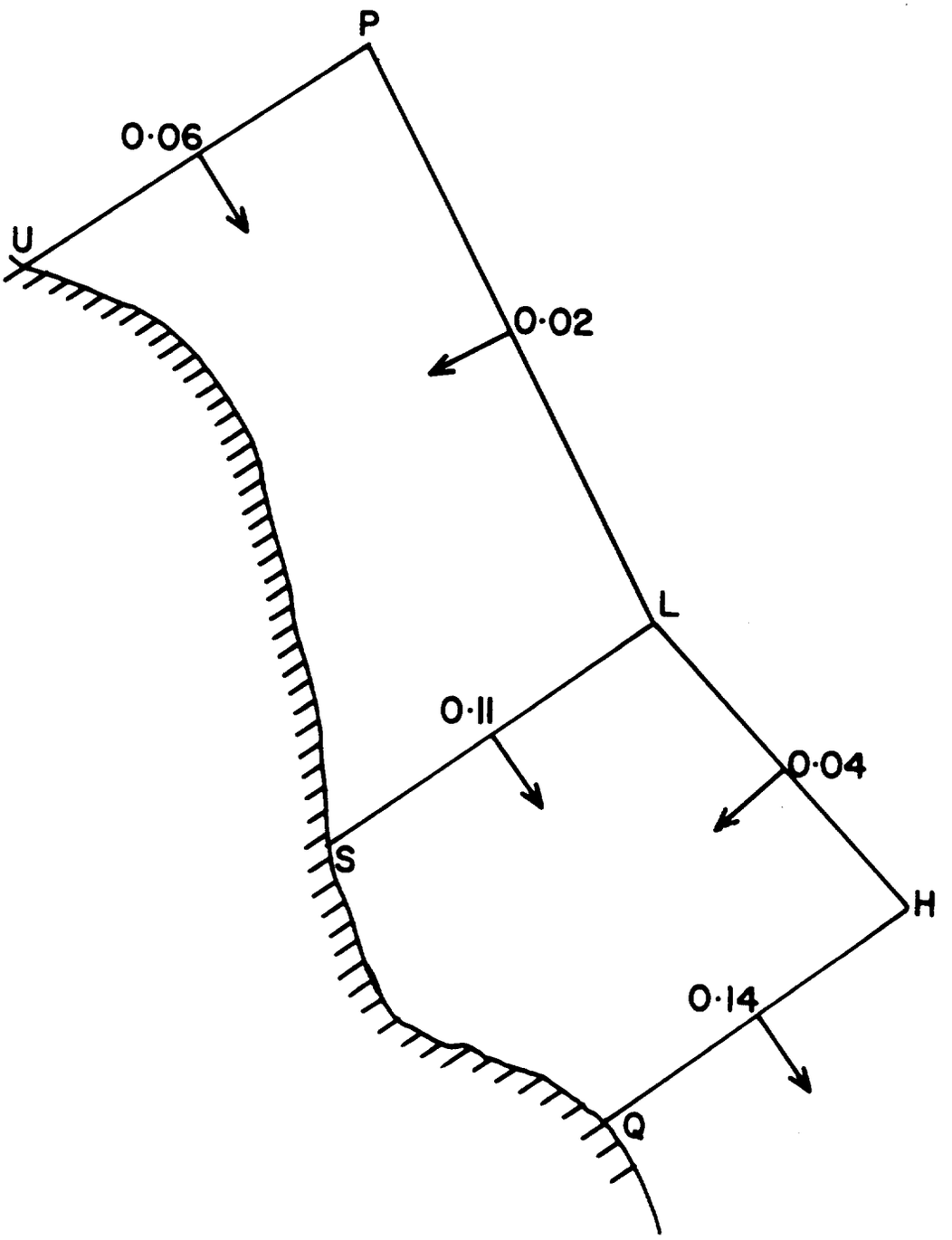

Figure 13. Energy flux for S2 with linear interpolations and extrapolations, over one tidal period. Units are 10^{10} Watts.

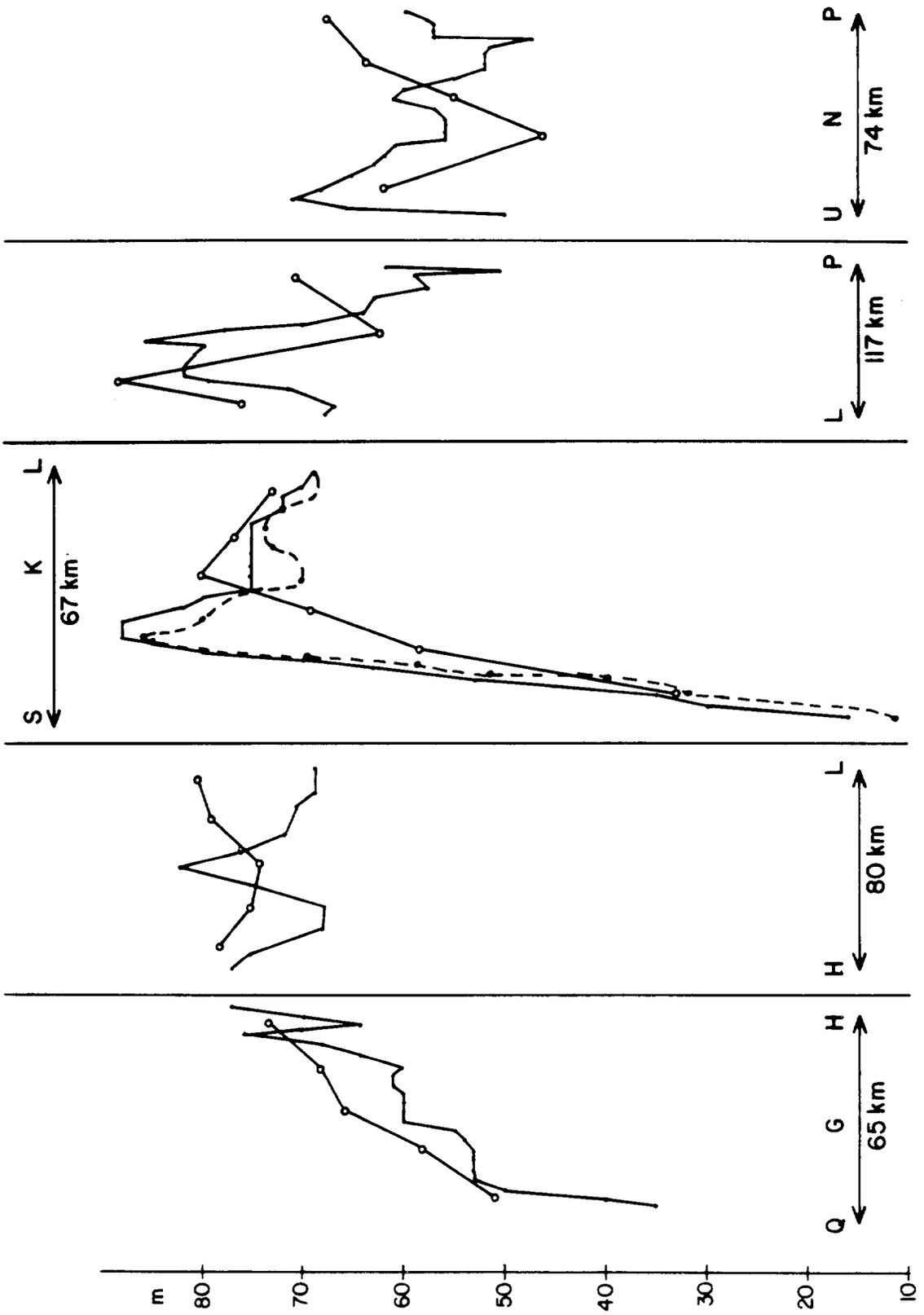

Figure 14. Comparisons between real and numerical depths along box boundaries.

o——— o numerical depths
——————— depths read from charts
•– – – – • modified depth profile for SKL

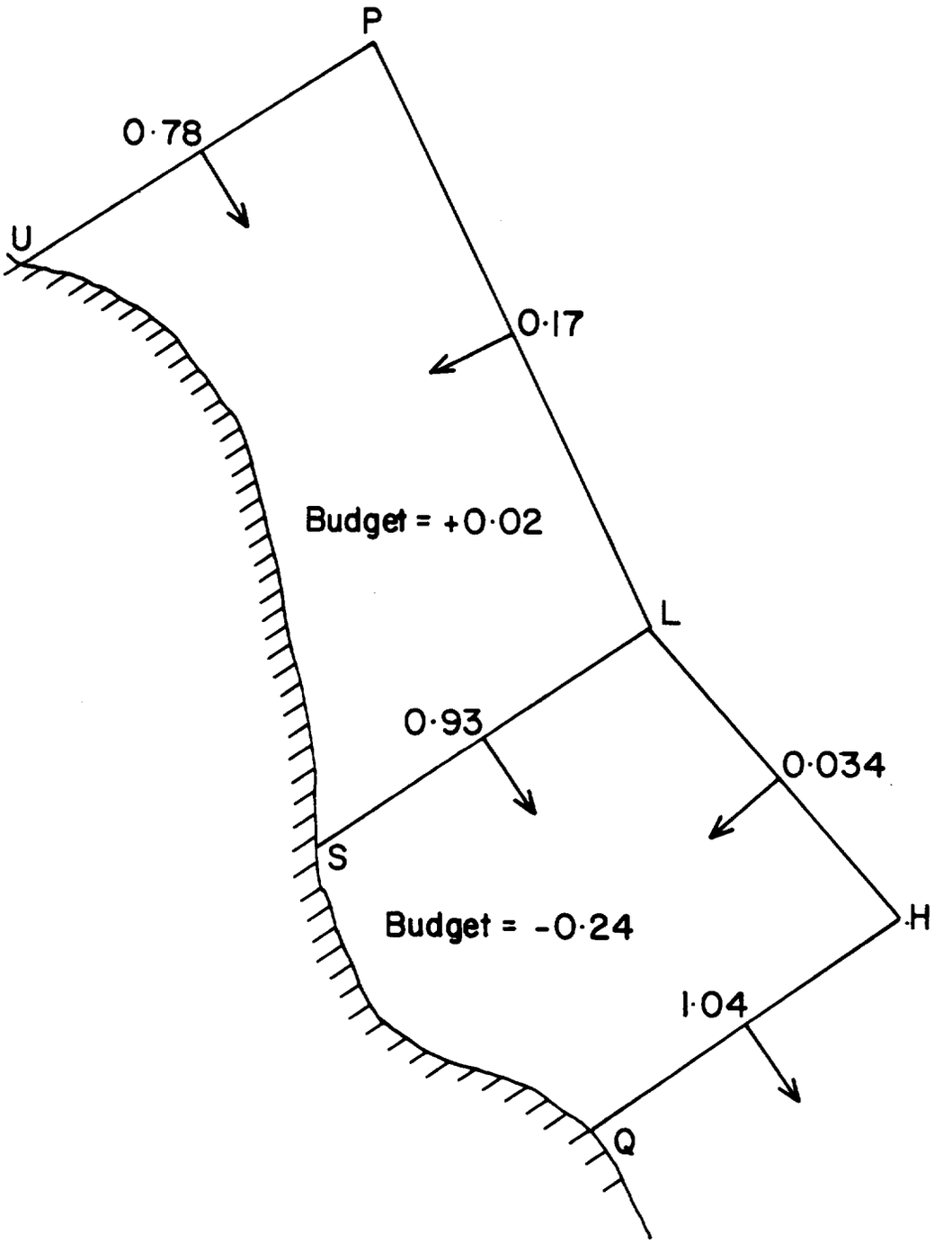

Figure 15. Numerical model energy fluxes modified to fit the lengths of the sides of the experimental boxes.

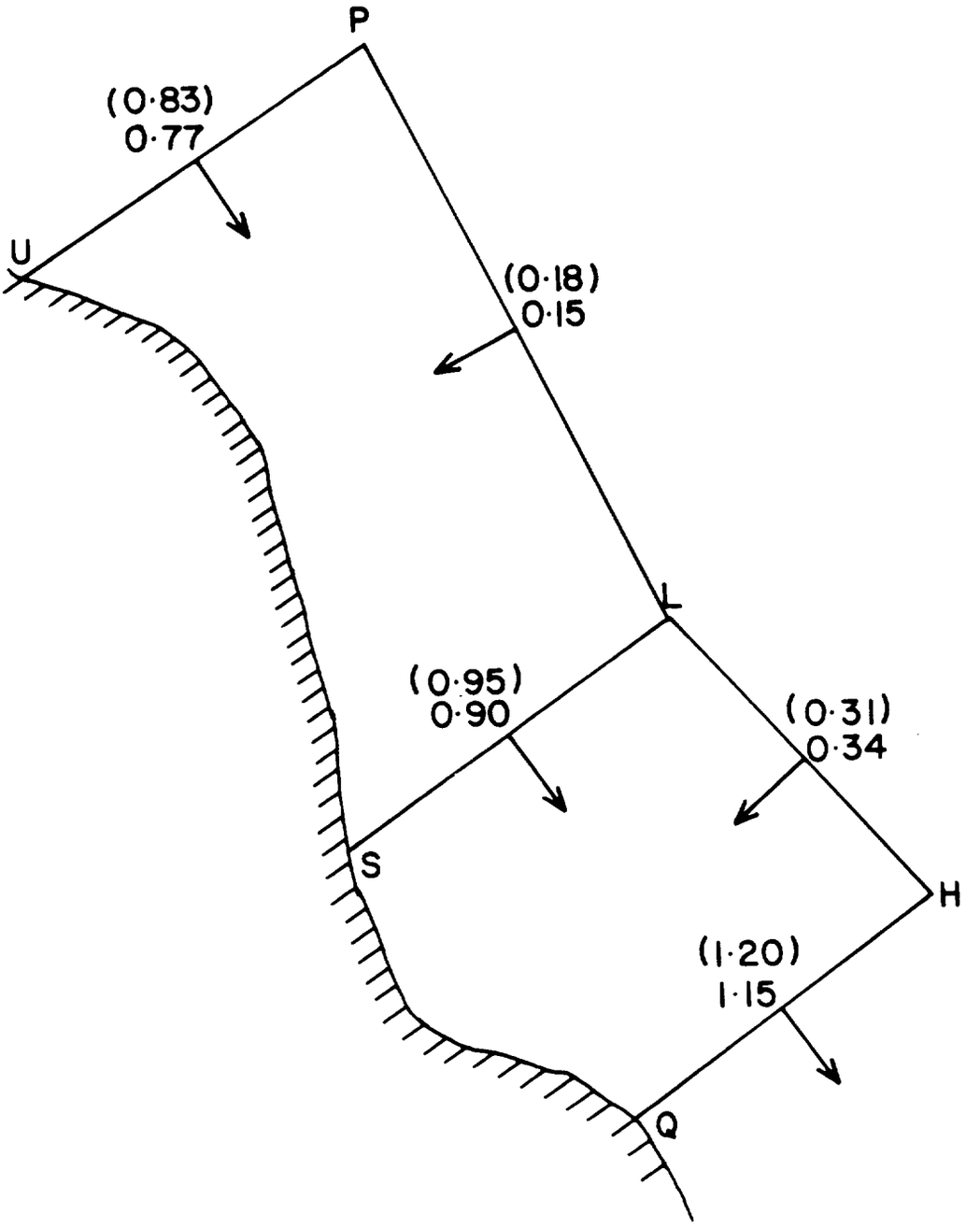

Figure 16. Comparison of the M2 energy fluxes from the observations and the numerical model. Numerical model values are bracketed. Units are 10^{10} watts.

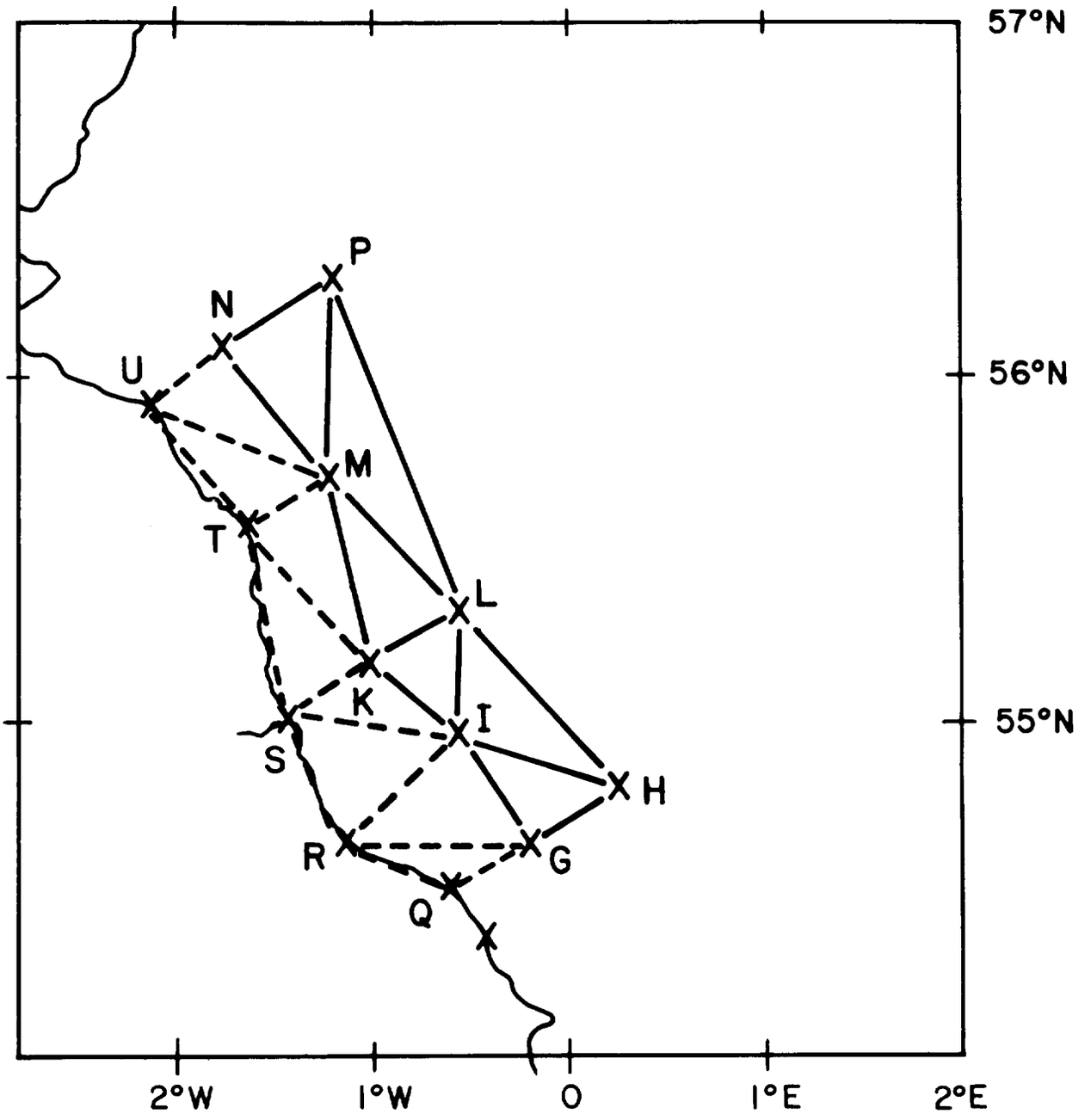

.gure 17. Triangular representation of the area of energy dissipation. Dashed lines connect to estimated coastal currents.

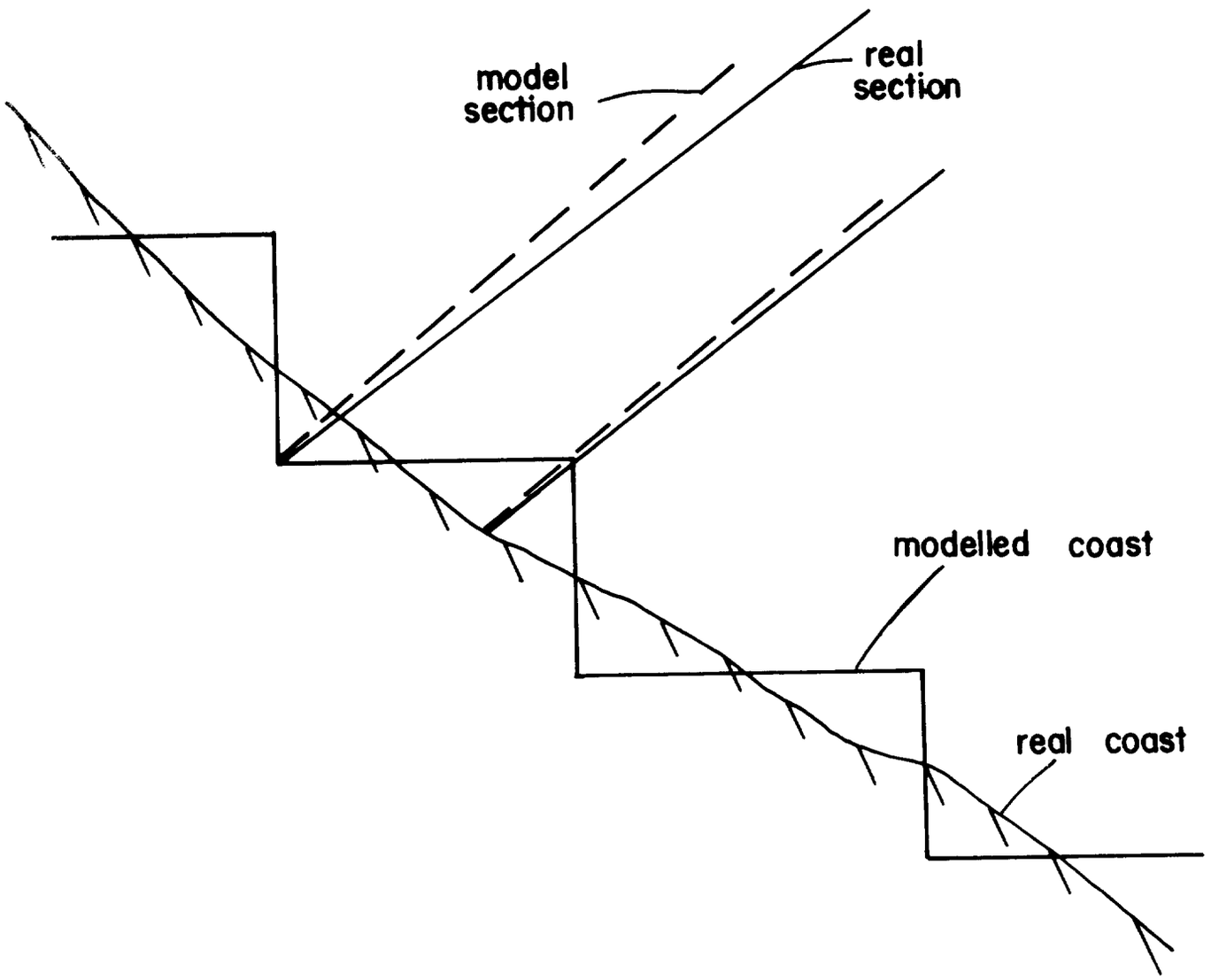

Figure 18. Showing the discrepancy between a real coastline and its numerical representation.